ARTICLE

Received 00th January 20xx, Accepted 00th January 20xx

DOI: 10.1039/x0xx000000x

Cu₄MnGe₂S₇ and Cu₂MnGeS₄: Two Polar Thiogermanates Exhibiting Second Harmonic Generation in the Infrared and Structures Derived from Hexagonal Diamond.

Jennifer R. Glenn,^a Jeong Bin Cho,^b Yiqun Wang,^c Andrew J. Craig,^a Jian-Han Zhang,^e Marvene Cribbs,^a Stanislav S. Stoyko,^a Kate E. Rosello,^a Christopher Barton,^a Allyson Bonnoni,^a Pedro Grima-Gallardo,^{e,f} Joseph H. MacNeil,^g James M. Rondinelli,^c Joon I. Jang,^b and Jennifer A. Aitken^a

The new, quaternary diamond-like semiconductor (DLS) Cu₄MnGe₂S₇ was prepared at high-temperature from a stoichiometric reaction of the elements under vacuum. Single crystal X-ray diffraction data were used to solve and refine the structure in the polar space group Cc. Cu₄MnGe₂S₇ features [Ge₂S₇]⁶⁻ units and adopts the Cu₅Si₂S₇ structure type that can be considered a derivative of the hexagonal diamond structure. The DLS Cu₂MnGeS₄ with the wurtz-stannite structure was similarly prepared at a lower temperature. The achievement of relatively phase-pure samples, confirmed by X-ray powder diffraction data, was nontrival as differential thermal analysis shows an incongruent melting behaviour for both compounds at relatively high temperature. The dark red Cu₂MnGeS₄ and Cu₄MnGe₂S₇ compounds exhibit direct optical bandgaps of 2.21 and 1.98 eV, respectively. The infrared (IR) spectra indicate potentially wide windows of optical transparency up to 25 μm for both materials. Using the Kurtz-Perry powder method, the second-order nonlinear optical susceptibility, $\chi^{(2)}$, values for Cu₂MnGeS₄ and Cu₄MnGe₂S₇ were estimated to be 16.9 ± 2.0 pm/V and 2.33 ± 0.86 pm/V, respectively, by comparing with an optical-quality standard reference material, AgGaSe₂ (AGSe). Cu₂MnGeS₄ was found to be phase matchable at λ =3100 nm, whereas Cu₄MnGe₂S₇ was determined to be non-phase matchable at λ =1600 nm. The weak SHG response of Cu₄MnGe₂S₇ precluded phase-matching studies at longer wavelengths. The laser-induced damage threshold (LIDT) for Cu₂MnGeS₄ was estimated to be \sim 0.1 GW/cm² at λ =1064 nm (pulse width: τ =30 ps), while the LIDT for Cu₄MnGe₂S₇ could not be ascertained due to its weak response. The significant variance in NLO properties can be reasoned using the results from electronic structure calculations.

Introduction

Infrared (IR) solid-state laser systems (SSLSs) serve many vital functions in the military, ^{1,2} medical, ^{3,4} and industrial sectors. ⁵ At the heart of these SSLSs is the nonlinear optical (NLO) crystal, which is the most critical and limiting component for efficient generation of IR radiation via several frequency conversion

- ^{a.} Department of Chemistry and Biochemistry, Duquesne University, Pittsburgh, PA 15282, USA.
- ^{b.} Department of Physics, Sogang University, Seoul, 04017, South Korea.
- C. Department of Materials Science and Engineering, Northwestern University, Evanston, IL, 60208-3108, USA
- ^d School of Resources and Chemical Engineering, Sangming University, Sanming, 365004, P.R. China
- e. Centro de Estudios de Semiconductores, Departamento de Físcia, Facultad de Ciencias, Universidad de Los Andes, Mérida, 5101, Venezuela.
- f. Centro Nacional de Tecnologías Ópticas (CNTO), Mérida, 5101, Venezeula.
- ^{g.} Department of Chemistry, Chatham University, Pittsburgh, PA 15232, USA.
- † Co-corresponding authors, Joon I. Jang, E-mail: jjcoupling@sogang.ac.kr and Jennifer A. Aitken, Email: aitkenj@duq.edu.

Electronic Supplementary Information (ESI) available: [X-ray crystallographic information file in CIF format; crystal data, data collection and structure refinement details; fractional atomic coordinates and equivalent isotropic displacement parameters; atomic displacement parameters; bond distances; bond angles; refinement models, extended connectivity table; simulated precession images, differential thermal analysis curves, ATR FT-IR spectra]. See DOI: 10.1039/x0xx00000x

processes.⁶ For example, ZnGeP₂ (ZGP) optical parametric oscillators (OPOs) have been used in IR countermeasure systems⁷ and cavity-ringdown spectroscopy for the detection of trace gases, such as the explosive TNT.⁸ A mid-IR hyperspectral imaging system for medical diagnostics has been realized using AgGaS₂ (AGS) as the NLO medium for sum frequency generation (SFG).⁹ Although there are many current uses of IR-NLO crystals, there remains a great need for improved materials that can function over a wider range of wavelengths, achieve higher efficiencies, and generate greater output powers in the mid-IR, in order to access new domain applications.¹

The obstacle to identifying new IR-NLO candidates is the difficulty in simultaneously achieving all desirable characteristics in one material. Some critical materials features are: 1) sufficient birefringence for phase matching (PM) over a wide region, 2) large NLO coefficient, 3) high laser-induced damage threshold (LIDT), 4) extreme transparency in the IR, and 5) the capability to produce sizeable single crystals without cracks, domain structures, or other absorption losses, among others. 10,11

The large majority of commercialized IR-NLO crystals are diamond-like semiconductors (DLSs), for example ZGP, AgGaSe₂ (AGSe), AGS, LiGaS₂ (LGS), LiInS₂ (LIS), LiGaSe₂ (LGSe) and LiInSe₂ (LISe). ZGP has a very large second-order NLO coefficient, $\chi^{(2)}$,

ARTICLE Dalton Transactions

of 150 pm/V; however, it has a narrow window of usage, 2 µm-8.5 µm, because of either absorption losses or multiphoton absorption (MPA) effects. 10,12 AGSe has a sizeable $\chi^{(2)}$ (66 pm/V) and a very wide region of optical transparency; however, it possesses a low LIDT and cannot be used in the near-IR (<3 µm) because it is not PM in that region. 10,13 While AGS is PM at 1.8 µm and has a decent $\chi^{(2)}$ (36 pm/V), it also has a relatively low LIDT. 11,14 The lithium-containing materials, LGS, LIS, LGSe and LISe, have higher LIDT values than the silver-containing DLSs, but the $\chi^{(2)}$ values are notably lower, ranging from ~7 to ~22 pm/V. 6,13,15,16 Therefore, it is necessary to investigate a variety of compounds in pursuing new options for next-generation, IR-NLO devices.

Chalcogenides are, arguably, the best materials for IR-NLO applications; they generally possess extensive, inherent optical transparency in the IR, relatively wide optical bandgaps that lead to favourable LIDTs, and highly polarizable bonds that give rise to sizeable optical nonlinearities. 10,17,18,19 discoveries have revealed that a number of chalcogenides with diverse crystal structures and chemical compositions are promising IR-NLO candidates. These include binary materials such as γ -In₂Se₃²⁰ and two polymorphs of Ga₂Se₃,^{21,22} ternary chalcogenides such as Ba_2SnS_5 , 23 Cd_4SiSe_6 , 24 $SnGa_4S_7$, 25 and BaGa₄Se_{7,}²⁶ and a plentiful collection of quaternary compounds. The large majority of the quaternary candidates contain an alkali metal, an alkaline-earth metal, a coinage metal, or a combination of these, for example, Na₂Ga₂TS₆ (T = Ge, Sn),²⁷ $NaGaln_2Se_5$, ²⁸ [RbBa₂Cl][Ga₄S₈], ²⁹ RbMSn₂Se₆ (M=Ga, In), ³⁰ SrA_2SiS_4 (A= Li, Na, Cu),³¹ $SrCdSnS_4$,³² $BaMnSnS_4$,³³ $Ba_{10}In_6Zn_7S_{10}Se_{16}$,34 BaGa₂GeSe₆,³⁵ Ba₁₃In₁₂Zn₇S₃₈,³⁶ Ba₆In₆Zn₄Se₁₉,³⁷ AgGaGeS₄,³⁸ and CuZnPS₄.³⁹ A special subclass of chalcogenides that has been the focus of our group⁴⁰⁻⁴⁶ and a others47-52 is DLSs possessing inherently noncentrosymmetric crystal structures, the primary criterion for second harmonic generation (SHG). To date, the best quaternary DLSs are Li₂ZnSiS₄,⁴⁸ Li₂CdSiS₄,^{43,52} Li₂MnGeS₄,⁴⁰ $\alpha\text{-Li}_2\text{ZnGeS}_4,^{41}\text{Li}_2\text{CdGeS}_4,^{42}\text{LiGa}_{0.54}\text{In}_{0.46}\text{S}_2,^{47}$ and $\text{Li}_4\text{CdSn}_2\text{S}_7,^{43}$

In this work, we report the linear and nonlinear optical properties, synthesis, crystal structure, thermal analysis, transparency, and calculated electronic structure of a new quaternary DLS of the less frequently encountered I₄-II-IV₂-VI₇ formula, namely Cu₄MnGe₂S₇. For comparison, the analogous I₂-II-IV-VI₄ compound, Cu₂MnGeS₄, was also prepared and characterized. Cu₂MnGeS₄⁵³ is an antiferromagnet with a Néel temperature, T_N , around 9K.⁵⁴ This compound has been highlighted as a promising magnetoelectric and multiferroic candidate,⁵⁵ and more recently, evaluated for its ability to sense γ-rays and neutrons.⁵⁶ Additionally, thin films of Cu₂MnGeS₄ have been prepared and studied in the context of solar energy conversion.⁵⁷ Here, we demonstrate that while Cu₄MnGe₂S₇ displays a weak SHG response, Cu₂MnGeS₄ generates a strong SHG response at room temperature. Some insights regarding the widely differing behaviour of these two DLSs containing the same elements but different stoichiometry, are offered based on results of the electronic structure calculations.

Experimental

Reagents

All chemicals were obtained from commercial sources and were not further purified. Copper powder packed under argon (99.999%, Strem) and sublimed sulphur powder (99.5%, Fisher Scientific) were used as obtained. Large plate-like pieces of manganese (99.98%, Alfa Aesar) were washed with a solution of 10% nitric acid in methanol to remove surface oxidation, immediately taken into the glovebox, and ground to a fine powder using a DiamoniteTM mortar and pestle prior to use. Germanium chunks (99.999%, Strem) were similarly ground to a powder. All chemical reagents were stored and handled in a dry, argon-filled glovebox.

Phase-pure powder of Cu₂MnGeS₄

Phase-pure microcrystalline powder of Cu_2MnGeS_4 was prepared from a stoichiometric mixture of the elements, enough to prepare ~1.3 mmol of product. The reagents were combined, ground, and pressed into an 8 mm pellet using a carver pellet press implementing 2 metric tons of pressure. The pellet was subsequently inserted into a 12 mm o.d. fused-silica tube, evacuated to a pressure of ~10-4 mbar and flame-sealed using a methane-oxygen torch. The reaction was heated from room temperature to 850 °C in 12 h, held at 850 °C for 168 h, cooled from 850 to 650 °C at a rate of 2 °C/h, and further cooled to room temperature radiatively. The product consisted of a deep-red, sintered pellet that was subsequently ground to a microcrystalline powder.

Single crystals of Cu₄MnGe₂S₇

Single crystals of $\text{Cu}_4\text{MnGe}_2\text{S}_7$ were prepared in a similar manner as the phase-pure $\text{Cu}_2\text{MnGeS}_4$ powder described above with a few exceptions. The reaction was carried out with enough material to prepare ~0.7 mmol of product. The high-temperature hold was at 900 °C and the cooling was performed from 900 °C to 300 °C at a rate of 6 °C/h. After breaking the sintered pellet apart, small, deep-red, polyhedral-shaped single crystals, ~0.1-0.2 mm on an edge, were found using an optical microscope. X-ray powder diffraction analysis showed that $\text{Cu}_4\text{MnGe}_2\text{S}_7$ was the major reaction product; however, $\text{Cu}_2\text{MnGeS}_4$ and Cu_2GeS_3 were also indicated as well as several small peaks that could not be indexed to any known phase.

Phase-pure powder of Cu₄MnGe₂S₇

Phase-pure microcrystalline powder of $Cu_4MnGe_2S_7$ was prepared in a manner similar to Cu_2MnGeS_4 described above with several differences. The reaction was carried out to produce 2 mmol of product and the reagents were shaken (not ground) before pressing into a pellet. The high-temperature hold was at 1075 °C for 216 h, and the slow cooling step was carried out from 1075 to 875 °C at a rate of 2 °C/h. The product consisted of a reddish black ingot that was subsequently ground to a powder.

Single crystal structure determination

Dalton Transactions ARTICLE

A single crystal was selected under an optical microscope and, using Krazy[™] glue, it was adhered to a glass fibre that was held in a brass specimen pin using wax. The pin was then inserted into a goniometer head and single crystal X-ray diffraction data were collected at room temperature using a Bruker SMART APEX2 CCD single crystal X-ray diffractometer employing Mo K_{α} radiation, at a wavelength of λ =0.71703. The APEX2 software was used to execute the data collection, where three $\,\omega$ scans and one $\,\phi$ scan covering over a hemisphere of reciprocal space were carried out. The data reduction and final unit cell refinement were accomplished using SAINT.⁵⁸ An absorption correction (multi-scan type) was implemented using SADABS⁵⁹ and the files were set up for SHELX using XPREP.60 The systematic absences indicated two possible space groups, Cc (No. 9) and C2/c (No. 15); however, the structure could only be solved and refined in the polar, noncentrosymmetric space group Cc. All DLSs lack an inversion centre because all of the tetrahedral units align along the same crystallographic direction. Furthermore, the presence of an SHG signal supports the noncentrosymmetric space group. SHELX9761 and the shelXle graphical user interface⁶² were used to solve and refine the structure. Extinction was included in the refinement (0.00567(18)). Abbreviated and full tables of crystallographic data and structure refinement details for Cu₄MnGe₂S₇ can be found in Table 1 and Table S1, respectively. Fractional atomic coordinates, isotropic displacement parameters, atomic displacement parameters, bond distances and bond angles are located in Tables S2-S6. Simulated precession images are provided in Figure S1. The CIF file is deposited with the Cambridge Structural Database (CSD 2098932)

Table 1. Selected crystallographic and structure refinement details for Cu₄MnGe₂S₇.

Chemical Formula	Cu₄MnGe₂S ₇
Formula Weight	678.70
Space Group	<i>Cc</i> (No. 9)
α (Å)	16.7332(3)
b (Å)	6.4760(1)
c (Å)	9.8022(2)
β(º)	93.1517(9)
V (ų)	1060.60(3)
Z	4
$ ho_{calc}$ (g cm $^{-3}$)	4.250
Reflections measured	4396
Reflections independent (R_{int})	2405 (0.015)
Completeness to $\theta = 27.474^{\circ}$	100%
R1, wR2 $[I > 2\sigma(I)]$	0.0210, 0.0521
R1, wR2 (all data)	0.0223, 0.0551
GOF on F ²	1.068
Absolute Structure Parameter	0.063(12)

X-ray powder diffraction (XRPD)

Samples were primed for analysis by grinding in an agate mortar and pestle for five minutes and spreading the powdered material onto an oriented silicon-wafer, zero-background holder. A PANalytical X-Pert Pro MPD X-ray powder diffractometer employing Cu K_{α} radiation and functioning in Bragg-Brentano geometry at room temperature was used to collect data from 10 to 80° 20. The diffracted beam optics were

arranged with a 0.02 rad Soller slit, an anti-scatter slit of ½°, and a ¾° divergent slit. Between the sample and the X'Celerator detector, a 0.02 rad Soller slit, a ½° antiscatter slit and a nickel filter were used. Data were collected with a step size of ~0.008° and a scan speed of ~0.01°/s. The identification of crystalline phases was performed using the X'Pert HighScore Plus software⁶³ and the powder diffraction file (PDF)⁶⁴ database from the International Centre for Diffraction Data (ICDD).

Inductively Coupled Plasma Optical Emission Spectroscopy (ICP-OES)

Sample preparation and quantitative analysis were performed by a commercial materials characterization laboratory (RJ Lee Group Inc.). The title compounds were prepped for analysis by dissolving approximately 50 mg of each sample using a microwave-assisted acid-digestion procedure in high-pressure XP1500 vessels within a MARS Xpress CEM Microwave System. After digestion, quantitative ICP-OES was carried out for Cu, Mn, Ge and S by using EPA Method 6010C.

Differential thermal analysis (DTA)

Specimens were prepped for DTA by grinding, weighing (~20 mg) and inserting the powdered material into a carbon-coated, fused-silica ampoule, which was subsequently flamed-sealed under vacuum (10⁻³ mbar). Another ampoule of comparable mass was prepared using the reference material, Al₂O₃, which does not undergo any thermal transitions in the temperature range of the investigations. A Shimadzu DTA50 Differential Thermal Analyzer, calibrated using a three-point calibration curve, was used for data collection. The sample and the standard were simultaneously heated from room temperature to 1100 °C at a rate of 10 °C/min, held at 1100 °C for 1 min, and then cooled to 100 °C using a ramp of 10 °C/min. A second cycle was performed to assess the reproducibility of the thermal events. The temperatures labelled in the DTA diagrams were obtained by extrapolation of the peak of the thermal event to the baseline of the heating curve.

Diffuse reflectance UV-vis-NIR spectroscopy

Samples were prepared for measurements by grinding and inserting into the sample cup that was preloaded with powdered BaSO₄, the 100% reflectance standard. Optical diffuse reflectance data were collected from 200 to 2500 nm (600 nm/min) using a Varian Cary 5000 spectrometer furnished with a Harrick Praying Mantis Diffuse Reflectance Accessary. The Kubelka-Munk equation⁶⁵ was used to transform the reflectance data to absorption.

Attenuated total reflectance (ATR) Fourier transform (FT) – infrared (IR) spectroscopy

Samples were ground prior to ATR FT-IR measurements. Data were acquired with a Thermo Nicolet 380 FT-IR Spectrometer fitted with an ATR accessory. The OMNIC software was employed for both data collection and analysis. In transmission mode, 512 scans were collected over a range of 400-4000 cm $^{-1}$. In this configuration, a diamond-crystal makes optical contact with the specimen, leading to an $^{\sim}2~\mu m$ penetration depth,

ARTICLE Dalton Transactions

close to the lower limit of the particle size of the powdered samples. Therefore, the influence of thickness on the intensity is deemed inconsequential.⁶⁶

Second-order nonlinear optical (NLO) property measurements

Microcrystalline powdered samples were prepared for NLO measurement by sieving using a set of W. S. Tyler[™] stainless steel test sieves. After shaking, powdered samples of size ranges <20 μ m, 20-45 μ m, 45-63 μ m 63-75 μ m, 75-90 μ m, 90-106 μ m, and 125-150 μ m were collected, placed into fusedsilica capillary tubes, evacuated to ~10⁻³ mbar and flame-sealed using a natural gas-oxygen torch. Although the compounds were deemed stable, they were sealed under vacuum to prevent exposure to air and moisture during measurements and storage. Each sample was loaded onto a homemade sample holder subsequently mounted on a Z-scan translation stage. The $\,$ SHG responses of the samples were compared to an opticalgrade, single-crystal reference sample of AGSe that was ground into a powder and prepared in a similar manner as the above samples under investigation. The optical-grade AGSe from Gooch and Housego generally gives an SHG response 2X that of our "homemade" microcrystalline AGSe. 40,42,45

An input wavelength of 3100 nm was used for the PM study of Cu₂MnGeS₄. When possible, we prefer to assess samples at long wavelengths, where both the sample and the reference become PM and the SHG responses plateau (i.e. static limit); however, the signal for $Cu_4MnGe_2S_7$ was too weak to be measured by the InGaAs detector at longer wavelengths. Therefore, an input wavelength of 1600 nm was used for the PM study of Cu₄MnGe₂S₇. This was the longest wavelength where the SHG response could be reasonably detected. Using a reflection geometry and a fibre-optic bundle, which was coupled to a spectrometer fitted with a CDD camera and the InGaAs detector, the SHG signals from the samples and the reference were collected. All NLO measurements were carried out at room temperature. The SHG response from other components, as well as surface-induced effects, were determined to be negligible. The repetition rate of the laser was 50 Hz; therefore, the thermal load to the sample was deemed inconsequential. Additional details about the excitation source are available elsewhere. 40,45 In addition to a very weak signal, Cu₄MnGe₂S₇ exhibited location-dependent SHG, presumably caused by sample inhomogeneity; therefore, the SHG counts were collected for ten indiscriminately selected spots with a collection time of 210 seconds. In comparison, the SHG response of AGSe was collected for only 5 seconds. The LIDT assessment for Cu₂MnGeS₄ was performed at 1064 nm, the primary wavelength used in picosecond difference frequency generation (DFG) in the mid-IR. The laser intensity was varied from 0.2 GW/cm² to 2.5 GW/cm² and the spot size was 0.5 mm. The pulse width, τ , for all NLO measurements was 30 ps. The LIDT could not be determined for Cu₄MnGe₂S₇ due to its poor SHG response.

Electronic structure calculations

Electron band structure and density of states (DOS) calculations were carried out using density functional theory (DFT)

implemented in the Vienna *Ab initio* Simulation Package (VASP). 67,68 The Perdew-Burke-Ernzerhof generalized gradient approximation (PBE-GGA) 69 was used to treat the exchange and correlation effects. A 500 eV planewave cut-off and projector augmented-wave (PAW) pseudopotentials 70 were used for all elements, with the following valence electron configurations: $\text{Cu}(3d^{10}4s^1)$, $\text{Mn}(3d^64s^1)$, $\text{Ge}(3d^{10}4s^24p^2)$ and $\text{S}(3s^23p^4)$. The Γ -centred k-point meshes and $2\times 4\times 3$ and $4\times 4\times 4$ grids were used for $\text{Cu}_2\text{MnGeS}_4$ and $\text{Cu}_4\text{MnGe}_2\text{S}_7$, respectively. A Gaussian smearing with a width of <5 meVÅ $^{-1}$ was used for sampling and integrations within the Brillouin zone. The tetrahedron method with Blöchl corrections was applied for the calculation of the DOS.

Full lattice relaxations were executed until the residual forces on the individual atoms were >5.0 meVÅ-1. Because Cu_2MnGeS_4 has been shown to display antiferromagnetic (AFM) spin order, spin-polarized calculations with opposite spins on neighbouring Mn atoms (i.e. in a G-type AFM configuration), were utilized. On-site Coulomb interactions were not required owing to the half-filled d^5 and fully-filled d^{10} electronic configurations of the Mn and Cu ions, respectively. Spin-orbit interactions were not considered in the simulations. For the reason that semi-local DFT functionals are notorious for underestimating the electronic bandgap of semiconductors and insulators, 71 we also computed and compared the bandgaps of the two compounds using the range separated hybrid functional HSE06. 72

Results and discussion

Crystal structures

The crystal structures of DLSs are related to either cubic or hexagonal diamond. The latter, also named Lonsdaleite, was originally identified in meteorite samples in 196773,74 and recently prepared at extremely high pressures.75,76 Yet DLSs with structures derived from the rare hexagonal diamond are quite common. Figure 1 displays the honeycomb pattern found in wurtzite-type MnS and the title compounds, Cu₂MnGeS₄ and Cu₄MnGe₂S₇, all of which adopt structures descended from that of hexagonal diamond. These structures can be envisioned as an ordered arrangement of cations and anions over the carbon sites in diamond, where each cation is tetrahedrally coordinated by four anions and vice versa. As the number of cations increases upon going from MnS to Cu₂MnGeS₄ and Cu₄MnGe₂S₇, a symmetry reduction is observed from hexagonal to orthorhombic and monoclinic, respectively. The structure of Cu₄MnGe₂S₇ crystallizes in the lowest symmetry space group for DLSs based on hexagonal closest packing.

Figure 2 shows the corner-sharing, metal-sulphur tetrahedra of the title compounds. The noncentrosymmetric nature of the structures is quite apparent from this view, as all of the tetrahedral building units are oriented along one crystallographic direction. Additionally, the different ordering patterns of the cations can be observed, where the structure of Cu₄MnGe₂S₇ possesses a more complex pattern than that of Cu₂MnGeS₄ and, as a consequence, a larger unit cell. While the

Dalton Transactions ARTICLE

MnS₄ tetrahedra in both of compounds are separated from one another, the GeS₄ tetrahedra are isolated from one another in only Cu₂MnGeS₄. For Cu₄MnGe₂S₇ the two crystallographically unique Ge atoms (Ge1 and Ge2) share a sulphur atom (S1) to create a $[Ge_2S_7]^{6-}$ moiety. In the structure of Cu₂MnGeS₄ each CuS₄ tetrahedron shares corners with four others to create layers in the ac-plane, see Figure 3. Alternatively in the structure of Cu₄MnGe₂S₇, a three-dimensional network is generated by CuS₄ entities that share corners with five or six others, see Figure 3.

Due to the fact that many structurally related DLSs, such as Cu₂ZnSnS₄ (CZTS),^{77,78} Cu₂ZnSnSe₄ (CZTSe),⁷⁸ and Cu₂ZnGeSe₄ (CZGSe),⁷⁹ possess cation disorder, the cation ordering pattern found in Cu₄MnGe₂S₇ was critically evaluated. The tendency for disorder in these compounds stems from the similar tetrahedral radii. The difficulty in discerning the disorder in a number of these systems lies in the similar X-ray scattering cross-sections for some ions. In the case of Cu₄MnGe₂S₇, Cu⁺ and Ge⁴⁺ are isoelectronic and, therefore, difficult to distinguish by X-ray diffraction methods. There are seven crystallographically unique cation positions in the structure of Cu₄MnGe₂S₇, with copper and germanium residing on six of them. Thus, the Cu/Ge assignments were systematically switched in our structure refinement and the resulting statistics were recorded. The best model, reported here, had an R1/wR2 values 0.84/2.53% lower than that of the next best model. For Cu₄MnGe₂S₇ there is no other arrangement of the cations on those seven sites that results in R factors rivalling those in our reported structure here. Additionally, we attempted to introduce Cu/Ge disorder on each of the Cu and Ge sites, but did not achieve acceptable refinement statistics. However, we cannot rule out the presence of some Cu/Ge disorder without having neutron diffraction data, which requires a very large sample size. Furthermore, it should be noted that while the average Cu-S and Ge-S bond distances of 2.322(7) Å and 2.236(4) Å, respectively, are similar, examination of the individual bonds presents a different scenario. The four Cu-S bonds in each tetrahedron are comparable and the average bonding distances for each of the crystallographically unique Cu atom are also alike. On the other hand, the [Ge₂S₇]⁶⁻ unit has six short Ge-S bonds and two longer bonds to the bridging sulphur atom, 2.295(2) Å and 2.312(2) Å for Ge1-S1 and Ge2-S1, respectively. Therefore, while the long Ge-S bonds are relatively close to the average Cu-S bond, the average of the short Ge-S bonds, 2.213(4) Å, is noticeably smaller than the average Cu-S bonds, see Table S6.

Many aspects of diamond-like structures can be understood using Pauling's principles. ⁸⁰ The first principle explains that the coordination number in a structure is determined by the radius radio, r/ $_r$ -. The geometrically determined maximum radius ratio given by Pauling for a tetrahedron only holds for relatively hard ions and does not strictly predict the coordination for the relatively soft sulphides. ⁸¹ Yet, this rule still helps to explain why Mn²⁺ can be found in diamond-like materials, such as the title compounds, but not the much larger Pb²⁺. The third of Pauling's

tenets states that the presence of shared edges and shared faces in a structure tends to decrease its stability more than the sharing of corners. This justifies the high stability of the diamond structure, which has only shared corners among the tetrahedral building units, minimizing the distance between positively charged cations. The second and fourth of Pauling's theories are of particular importance in describing the structure of $\text{Cu}_4\text{MnGe}_2\text{S}_7$ and require more detailed discussion.

Pauling's second principle predicts that the charge of the anion should be balanced by the cations that are in its first coordination sphere in order for a coordination polyhedron to be regular. This is the case in the structure of Cu₂MnGeS₄, where every S2- is surrounded by two Cu+, one Mn2+ and one Ge4+. On the other hand, local electroneutrality is not satisfied by all of the S2- anions in the structure of Cu₄MnGe₂S₇ or other I₄-II-IV₂-VI₇ compounds such as Li₄CdSn₂S₇⁴³ and Cu₄ZnGe₂Se₇.⁸² Construction of an extended connectivity table shows that only S2, S3, S4 and S5 have their charges counterbalanced by the nearest neighbour cations, see Table S7. The S1 atom, which is coordinated by two Cu⁺ and two Ge⁴⁺, is overcompensated in terms of charge, whereas S6 and S7 are undercompensated, being bound to three Cu⁺ and one Ge⁴⁺. It is predicted that when local charge balance is not attained, the structure will distort. The cation-anion bonds will respond by lengthening or shortening for anions that are overcompensated or undercompensated, respectively. This effect is obvious for S1, which has an excess positive charge of 0.5. The longest Cu1-S, Cu2-S, Ge1-S and Ge2-S bonds are with S1, Table S4. The local charge of S6 and S7 is slightly negative, -0.25; thus, the influence of this deficiency on the bond distances is minor, Table S4.

Pauling's fourth principle concerns structures composed of different cations, such as the title compounds. In these structures, he proposed that the cations with the highest valence will tend not to share the corners, edges or faces of their polyhedra, in order to widen the separation between the highly charged cations. This explains why the GeS₄ tetrahedra are isolated from one another in all of the diamond-like structures adopted by the I₂-II-IV-VI₄ DLSs,⁸¹ such as Cu₂MnGeS₄. Conversely, the GeS₄ tetrahedra in Cu₄MnGe₂S₇ share a corner to form the [Ge₂S₇]⁶⁻ moiety. This may be influenced by the stoichiometry of the compound. On the other hand, a recent publication by George et al. examined the predictive power of Pauling's rules and found that many compounds violate the fourth principle.83 In these cases, they proposed that, "covalent and electronic-structure effects might be more important than electrostatics in these compounds."83

While the I_2 -II-IV-VI $_4$ compounds, such as Cu_2MnGeS_4 , follow Pauling's second and fourth rules, the I_4 -II-IV $_2$ -VI $_7$ compounds depart from them, demonstrating the amazing stability and high flexibility of the diamond structure. It is astonishing that the distortions predicted for the I_4 -II-IV $_2$ -VI $_7$ compounds turn out to be very subtle and average out over the entire structure yielding typical average bond distances and average bond angles of the expected 109.5°.

To further investigate the structures of the title compounds, the bond-valence-bond-length correlation was examined by applying the bond valence model developed by Brown.⁸⁴⁻⁸⁶ The

ARTICLE Dalton Transactions

bond valence sum, BVS, is defined as the sum of each bond valence, S_{ij} , within a coordination polyhedron, Eq(1).

$$BVS = \sum_{i} s_{ij} \tag{1}$$

In DLSs, where all atoms are tetrahedrally coordinated, four s_{ij} values are added to determine the BVS for each crystallographically unique atom. The individual s_{ij} values are found using,

$$s_{ij} = e^{\frac{(R_0 - R_{ij})}{b}}, (2)$$

where R_0 and b are empirically determined bond valence parameters, and R_{ij} is the experimentally determined bond length between atoms i and j. The discrepancy between the BVS and the expected atomic valence, v_i , provides a measure of the strain in the crystal structure, which is usually described by the global instability index (G) that can be calculated using

$$G = \sqrt{\frac{\sum_{i=1}^{N} (BVS - v_i)^2}{N}},$$
 (3)

where N is the number of atoms in the formula unit. Take heed that Brown explicitly states that N should not be taken as the number of atoms in the asymmetric unit, which may or may not agree with the formula unit. Therefore, in order to properly calculate the G values, it is necessary to consider the multiplicity of each crystallographically unique atom in the structure. In other words, if a crystal structure contains atoms having different site symmetries, each atom cannot be equally weighted when determining the G value. In the case of $\operatorname{Cu_2MnGeS_4}$ the $\operatorname{Cu1}$ and $\operatorname{S1}$ atoms lie on $\operatorname{4b}$ sites, while the other atoms reside on 2a sites; therefore, the $(BVS-v_i)^2$ value for $\operatorname{Cu1}$ and $\operatorname{S1}$ must be added twice, and the other atoms only once, in the summation. In this case, the value for N is 8, while the number of crystallographically unique atoms, i.e. number of atoms in the asymmetric unit, is only 6.

To understand the results (Table S8), it is important to know that a G value less than 0.05 is thought to arise from the unavoidable uncertainties of experimentally determined bond lengths. When the G value falls within the range of 0.05-0.20, the structure is considered to have an acceptable level of strain. A G value greater than 0.2 indicates a highly strained, unstable compound with possibly an incorrect structure determination. The G values determined for Cu₂MnGeS₄ and Cu₄MnGe₂S₇, using equation 3, were 0.18 and 0.19, respectively, signifying reasonable degrees of strain in these structures, Table S8.

X-ray powder diffraction, composition analysis and synthesis

The phase purity of the bulk reaction products was carefully evaluated using X-ray powder diffraction data. DLSs derived from the same form (i.e., cubic or hexagonal) of diamond commonly exhibit strikingly similar X-ray powder diffraction patterns containing many overlapping, or nearly overlapping, peaks. This phenomenon is clearly exemplified in the top and middle plots drawn in Figure 4, which shows the entire collected and the corresponding section of the calculated X-ray powder diffraction patterns for Cu₂MnGeS₄ and Cu₄MnGe₂S₇. However, close, careful data comparison determined that the two materials were prepared in relatively phase-pure form. This conclusion is more convincingly supported upon viewing the

enlargement of a few selected regions on the pattern displayed in the bottom of Figure 4. The phase-purity was further corroborated using ICP-OES, yielding compositions of $\text{Cu}_{1.94(5)}\text{Mn}_{1.00(3)}\text{Ge}_{1.01(3)}\text{S}_{4.0(1)}$ and $\text{Cu}_{4.06(6)}\text{Mn}_{1.00(1)}\text{Ge}_{2.01(3)}\text{S}_{7.05(5)}$ for $\text{Cu}_2\text{MnGeS}_4$ and $\text{Cu}_4\text{MnGe}_2\text{S}_7$, respectively.

Our synthesis procedure to prepare phase-pure Cu₂MnGeS₄ was similar to that found in previous literature reports, albeit with a couple of deviations. One difference is that our hightemperature hold was 50 °C higher. Secondly, while we did press the reactants into a pellet, as did Bernert and Pfitzner,87 we did not need to conduct multiple regrind-reheat cycles to achieve phase purity. In order to achieve high-quality results for Cu₄MnGe₂S₇, numerous reaction trials were conducted and the resulting products were evaluated. From this work, two parts of the reaction procedure were deemed particularly important for obtaining microcrystalline powder samples without the inclusion of secondary phases. One critical parameter was the reaction temperature. In the case of Cu₄MnGe₂S₇, reactions executed at temperatures in the range of 750-1050 °C resulted impure samples. At lower reaction temperatures, Cu₄MnGe₂S₇ was usually the predominant phase. However, Cu₂MnGeS₄ and Cu₂GeS₃ were also present, often in significant amounts; therefore, it was crucial to use high temperatures around 1075 °C. Additionally, the grinding of reactants tended to result in material sticking to the mortar and pestle, and those reactions did not yield phase-pure material. Instead, the best results were obtained when the reactants were gently mixed by shaking and pressed into pellets for subsequent heating.

Differential thermal analysis (DTA)

Differential thermal analysis was carried out in order to understand the thermal stability of Cu₂MnGeS₄ and Cu₄MnGe₂S₇. At least two thermal studies of Cu₂MnGeS₄ have been previously conducted. In 1977, Schäfer and Nitsche reported that Cu₂MnGeS₄ melts congruently at 994 °C.88 However, a higher melting temperature of 1014 °C was later reported by Bernert et al., who specifically mentioned using the "onset points in the thermal measurements".87 Unfortunately, the thermograms from which the conclusions of both studies were drawn were not published. The DTA diagrams for Cu₂MnGeS₄ and Cu₄MnGe₂S₇ are depicted in the top and bottom of Figure 5, respectively, as well as Figure S2. The analysis of the DTA data reported here provides additional information about the thermal behaviour of Cu₂MnGeS₄. Upon Cu₂MnGeS₄ undergoes two closely spaced endothermic events at 1011 and 1018 °C, close to the melting point observed by Bernert and coworkers.87 Upon cooling, Cu₂MnGeS₄ undergoes two exothermic events at the same temperatures. From this thermogram we conclude that Cu₂MnGeS₄ melts incongruently and is an intermediate compound in the $(Cu_2GeS_3)_{1-x}(MnS)_x$ phase diagram with x=0.5, since the solidification and the melting points coincide. Cu₄MnGe₂S₇ also melts incongruently with the melting and solidification points occurring at 961 and 934 °C, respectively. Cu₄MnGe₂S₇ is an intermediate compound in the (Cu₂GeS₃)₁₋ $_{x}(MnS)_{x}$ phase diagram with x=0.33. Prior to the complete melting of the sample, there is a solid-plus-liquid region, which Dalton Transactions ARTICLE

forms around 908 °C. Additionally, an order-disorder phase transition is observed at lower temperature, 679 °C upon heating and 666/681 °C upon cooling. Phase transitions are not uncommon for DLSs. These studies indicate that the single crystal growth of these two compounds may be quite challenging because they exhibit relatively high thermal stability, melt incongruently and undergo phase transitions.

UV-vis-NIR and FT-IR spectroscopy

Optical diffuse reflectance data were collected and converted to absorption for Cu₂MnGeS₄ and Cu₄MnGe₂S₇. Both compounds exhibit relatively clean absorption edges, as is expected based on their X-ray powder diffraction patterns that demonstrate phase-pure materials. The absorption edges exhibit a diffuse tail, known as the Urbach tail, which is commonly displayed in the optical absorption spectrum of a semiconductor and originates from defect states within the electronic band structure due to crystal defects and/or sample inhomogeneity.89 In order to properly assess the optical bandgaps, the Urbach tail regions were distinguished as the linear regions at the low energy side of the absorption edge when the log of the optical absorption data was plotted as a function of energy, Figure 6(left).89 Next, for each sample, the data above the Urbach tail area (>2.24 eV for Cu₂MnGeS₄ and >2.06 eV for Cu₄MnGe₂S₇) were fit using the functions for a direct and indirect bandgap semiconductor, $\alpha = A(E-E_a)^{1/2}/E$ and $\alpha = A(E-E_g)^2/E$, respectively, where A is a constant, E is the photon energy in electron volts and E_g is the bandgap energy. For semiconductor samples, a somewhat steep absorption edge points to a direct bandgap compound, while a gentler onset of the absorption edge is revealing of indirect behaviour. For both compounds, a larger linear region was encountered when applying the direct function, suggesting that the compounds possess direct bandgaps, Figure 6 (middle). For example, in the case of Cu₄MnGe₂S₇, the linear region for the direct bandgap fit spanned 0.18 eV, while the linear region for the indirect function fit covered 0.12 eV. Finally, the extrapolation of the direct function fit to the energy axis gave the estimated optical bandgap values of 2.21 eV and 1.98 eV, for Cu_2MnGeS_4 and Cu₄MnGe₂S₇, respectively, Figure 6 (right). These values, which correspond to 561 nm and 626 nm, tend to agree with the observed red colour of the samples, with Cu₄MnGe₂S₇ being of a noticeably darker red colour. A recent publication on the first thin film Cu₂MnGeS₄ samples reported an optical bandgap around 1.7 eV⁵⁷ and a narrower bandgap of 1.66 eV was reported at room temperature for Cu₂MnGeS₄ single crystals grown via chemical vapour transport.⁹⁰

An attractive feature of chalcogenide materials is their inherently high transparency over much of the IR region and in particular the key atmospheric windows. The attenuated total reflectance data converted to transmission are illustrated in Figure S3. Both compounds seem to exhibit potentially wide transparency regions that can be better assessed when they are prepared as large single crystals.

Second harmonic generation (SHG) and phase matching (PM)

Figure 7 displays the PM performance of Cu₂MnGeS₄ and Cu₄MnGe₂S₇, along with the optical-quality reference material, AGSe. Note well that the Kurtz-Perry powder method⁹¹ does not allow one to establish the type of PM. The SHG counts increase with increasing particle size range in the case of both Cu_2MnGeS_4 and AGSe at λ =3100 nm, indicating that the sample and the reference are PM at this wavelength, Figure 7 (top). The SHG signal for Cu₄MnGe₂S₇ was too weak to measure at relatively long wavelengths; thus, the PM behaviour was evaluated at λ =1600 nm. Neither Cu₄MnGe₂S₇ nor AGSe are PM at 1600 nm as indicated by the decrease in SHG counts with increasing particle size range, Figure 7 (bottom). Yet, Cu₄MnGe₂S₇ demonstrates a small increase for the particle sizes greater than 63-75 μm, which might be due to an oscillating PM factor.91 From this data we can infer that the coherence length of Cu₄MnGe₂S₇ is longer than that of AGSe. Although it was not possible to ascertain the experimental coherence length for Cu₄MnGe₂S₇, it is assumed to be below 20 μm.

The second-order NLO susceptibility, $\chi^{(2)}$, of Cu₂MnGeS₄ was assessed at λ =3100 nm, where both the sample and the standard are PM and MPA is insignificant. The estimated non-resonant $\chi^{(2)}$ value is essentially real with normal dispersion, i.e. the imaginary part of $\chi^{(2)}$ is negligible. Using the Kurtz-Perry powder technique,⁹¹ the near-static $\chi^{(2)}$ value for each sample, $\chi_{\rm S}^{(2)}$, was calculated using the established value of the optical quality reference, $\chi_{\rm R}^{(2)}$;

$$\chi_{S}^{(2)} = \chi_{R}^{(2)} \left(\frac{I_{S}^{SHG}}{I_{R}^{SHG}}\right)^{\frac{1}{2}}, \tag{4}$$

where I_S^{SHG} and I_R^{SHG} are the observed SHG counts from the sample and the reference, respectively. Given that $\chi^{(2)}$ is 66 pm/V for AGSe,¹³ the calculated $\chi^{(2)}$ value for Cu₂MnGeS₄ was determined to be 16.9 \pm 2.0 pm/V. Assuming that the coherence lengths of the sample and the reference are the same, equation 4 was also used to calculate a $\chi^{(2)}$ value of 1.63 \pm 0.17 pm/V for Cu₄MnGe₂S₇ for the smallest particle size range. It should be noted that this value of $\chi^{(2)}$ for Cu₄MnGe₂S₇ is not precise because the compound shows oscillation (Figure 7 bottom) and the coherence lengths of the sample and the reference are different. Thus $\chi^{(2)}$ values were determined using the measured SHG intensities for AGSe and Cu₄MnGe₂S₇ of every particle size range. The results, displayed in Figure 8, show a substantial uncertainty with a mean $\chi^{(2)}$ value of 2.33 \pm 0.86 pm/V.

To put these results into context, it is helpful to consider how these materials compare with the current commercially available NLO materials. In 1995, using a dataset of over 50 compounds, Jackson and team found a strong correlation between wide bandgaps and small $\chi^{(2)}$ values as well as narrow bandgaps and large $\chi^{(2)}$ values. Physical They derived two different power law expressions to fit the data in two bandgap energy intervals, $0 < E_g < 1.2$ eV and $1.2 < E_g < 8.4$. Using Jackson's power law expression for large bandgap materials, and $E_g = 2.05$ eV, the $\chi^{(2)}$ for ZGP is underestimated by about a factor of two. According to Jackson et al. this signifies that ZGP is a strong performer considering its bandgap energy. On the other hand, the title compounds, with bandgaps similar to ZGP, are weak

ARTICLE Dalton Transactions

performers based on the bandgap energy because the use of Jackson's formula results in severely overestimated $\chi^{(2)}$ values compared to those reported here. Bear in mind that several useful, commercially-available materials, such as KDP, are weak performers based on bandgap alone. Though deemed a weak performer, the $\chi^{(2)}$ of $\text{Cu}_2\text{MnGeS}_4$ is comparable with, or perhaps better than LIS with reported $\chi^{(2)}$ values ranging from 6.8 to 15 pm/V depending on preparation.⁶ Furthermore, the $\chi^{(2)}$ of $\text{Cu}_2\text{MnGeS}_4$ exceeds those of LGS and LGSe.¹³ To conclude, while the $\chi^{(2)}$ of $\text{Cu}_4\text{MnGe}_2\text{S}_7$ is very low, that of $\text{Cu}_2\text{MnGeS}_4$ is quite attractive and, therefore, the compound was further characterized in terms of LIDT.

Laser-induced damage threshold (LIDT)

In order to determine the LIDT for Cu₂MnGeS₄, the SHG counts of the sample with the largest particle size range were measured as a function of laser intensity at $\lambda = 1064$ nm, the wavelength used to report most LIDT values. Unfortunately, the LIDT could not be ascertained for Cu₄MnGe₂S₇ on account of its poor SHG response. Be aware that the AGSe reference exhibits two-photon absorption (2PA) at this wavelength and strong photoluminescence (PL), which has been previously documented. 43 Cu₂MnGeS₄ does not display PL under 2PA, suggesting that the relaxation pathways of optical excitation are essentially nonradiative.

The intensity-dependent SHG counts for the sample and the reference are drawn as blue triangles and black squares, respectively, in Figure 9. The blue and black dashed lines drawn in Figure 9 represent the ideal case, $I_{SHG} \propto I^2$, for Cu₂MnGeS₄ and the reference, respectively, when fundamental depletion by MPA is non-existent. One can see, however, that the collected SHG counts significantly depart from the dashed lines signifying strong 2PA in each case.

For the AGSe reference, the 2PA coefficient (β) was found by fitting the collected data using equation 5, where a is a proportionality constant related to the second-order nonlinearity and d is the particle size for our reflection geometry, $d=137.5\pm12.5~\mu m$. The 2PA fit for AGSe, depicted with a black solid curve, gives a value of β =40.0 \pm 3.4 cm/GW, in agreement with our previous experimental results, ^{42,93} as well as the theoretical value given by a two-band model within a factor of 2.94 The LIDT value of ~0.2 GW/cm² was found for AGSe by finding the input intensity where the 2PA fit (solid black curve) diverges from the ideal case (dashed black line).

$$I_{SHG} = \alpha \left(\frac{I}{1 + \rho dI}\right)^2, \tag{5}$$

On the other hand, the intensity-dependent SHG response of $\text{Cu}_2\text{MnGeS}_4$ is different from that of the AGSe reference and cannot be modelled using solely a 2PA fit. This is because $\text{Cu}_2\text{MnGeS}_4$ shows noticeable saturable absorption (SA), where the compound undergoes some depletion in its SHG response by 2PA at relatively low input laser intensity, but then resumes the square law tendency for higher intensities. The combination of 2PA and SA behaviour can be modelled using a modified version of the above equation,

$$I_{SHG} = \alpha \left(\frac{I}{1 + \beta dI / \left(1 + \frac{I}{I_{S}}\right)}\right)^{2}, \tag{6}$$

where I_S is the saturation intensity. Using equation 6, it was found that β =85.0 \pm 5.4 cm/GW and I_s = 3.4 GW/cm². Considering that Cu₂MnGeS₄ has a β value slightly more than twice that of the AGSe reference, the LIDT of Cu₂MnGeS₄ was assessed as approximately half that of AGSe, ~0.1 GW/cm². The phenomenon of SA has also been observed for a few other DLSs studied by our team, for example Li₂CdGeS₄, ⁴² and Li₄CdSn₂S₇, ⁴³ which possess higher LIDT values and wider bandgaps than the title compounds. The relatively low LIDT values for both Cu₂MnGeS₄ and the AGSe reference preclude their use in high powered laser applications but are reasonable given their bandgap values.

Electronic Structure Calculations

We performed *ab initio* DFT simulations to investigate the electronic structures of the title compounds. The band structure and projected density of states (DOS) of Cu_2MnGeS_4 and $Cu_4MnGe_2S_7$ using the PBE functional are shown in Figure 10 (a) and (b), respectively. Both materials were determined to exhibit G-type AFM spin configurations, and only the manganese ions show a $5\mu_B$ moment. As can be seen from Figure 10, the spin-up and spin-down channels are degenerate in both compounds.

It was determined that the title compounds each display a semiconducting bandgap at the semi-local DFT-PBE level: $0.64~\rm eV$ for $\rm Cu_2MnGeS_4$, and $0.5~\rm eV$ for $\rm Cu_4MnGe_2S_7$. The valence bands are relatively flat in both compounds with less than $0.5~\rm eV$ dispersion amplitude, while $\rm Cu_4MnGe_2S_7$ shows smaller dispersion compared with $\rm Cu_2MnGeS_4$. From the projected DOS we find that the valence bands mainly exhibit $\rm Cu_3$ and, to a lesser extent, $\rm S_3$ character. The contribution from manganese is small in the near-valence band region. These occupied $\rm 3d$ orbitals are lower in energy. There are a few conduction bands within $\rm 1~eV$ above the Fermi level, which are mainly formed by empty manganese $\rm 3d$ orbitals.

Both compounds possess a direct bandgap at the Γ point. Interestingly, $\text{Cu}_4\text{MnGe}_2\text{S}_7$ has flatter valence and conduction bands, but shows a significant band dispersion about Γ , which is not found for $\text{Cu}_2\text{MnGeS}_4$. The unit cell of $\text{Cu}_4\text{MnGe}_2\text{S}_7$ has a similar structure to the double cell of $\text{Cu}_2\text{MnGeS}_4$ with the same number of copper and germanium atoms, but missing one manganese atom and one sulphur atom. This could account for the comparable valence band structure paired with the dissimilar conduction band structure due to different atomic orbital contributions.

The electronic bandgaps calculated from the PBE functional are significantly smaller than the measured optical bandgap for both compounds with up to 75% error. Since it is well-known that semi-local DFT functionals are prone to underestimate the bandgap of semiconductors and insulators, we also used the range separated hybrid DFT functional HSE06. The inclusion of the short-ranged part of the Fock-exchange interaction

Dalton Transactions ARTICLE

alleviates the self-interaction problem in semi-local functionals. Owing to the high computational cost of HSE06, we did not compute the full band structure and bandgap of the two compounds. Instead, eigenvalues of the electronic Hamiltonian from selected k-points in the Brillouin zone were calculated and compared between PBE and HSE06. The difference in eigenvalues between the lowest conduction band and highest valence band at different k-points are shown in Tables S9 and S10 for the two title compounds. In general, HSE06 predicts quite reasonable bandgaps in both compounds, with 1.89 eV for Cu₂MnGeS₄ and 1.66 eV for Cu₄MnGe₂S₇. The relative errors in band gap are around 15% using the HSE06 functional, a significant improvement from the results obtained using the PBE functional. Furthermore, the difference in predicted gaps at various k-points between PBE and HSE06 are consistent in momentum space. Therefore, we expect that HSE06 could predict reasonable bandgaps with similar band structures to those from PBE.

Table 2. Comparison of experimental and calculated bandgap energies.

Compound	mpound Experimental E _g Calculated E _g		Calculated E _g	
	Direct fit	Direct (PBE)	Direct (HSE06)	
Cu ₂ MnGeS ₄	2.21 eV	0.64 eV	1.89 eV	
Cu ₄ MnGe ₂ S ₇	1.98 eV	0.50 eV	1.66 eV	

Conclusions

Both Cu₂MnGeS₄ and Cu₄MnGe₂S₇ have structures related to hexagonal diamond, wide windows of optical transparency in the IR, relatively high thermal stability, and direct bandgaps in the vicinity of 2 eV. However, while the title compounds are comprised of the same elements and have many similarities, their NLO behaviours are strikingly different. While Cu₄MnGe₂S₇ displays weak SHG, $\chi^{(2)}$ =2.33±0.86 pm/V, and is not PM at 1600 nm, Cu₂MnGeS₄ has a sizeable $\chi^{(2)}$ value of 16.9±2.0 pm/V and is PM at 3100 nm. A similar disparity in NLO properties was observed for Cu₂ZnGeSe₄ and Cu₄ZnGe₂Se₇ with structures derived from cubic diamond.⁸²

The electronic structure calculations show some dissimilarities in the band dispersions of the title compounds. These features in turn affect the virtual excitations that impact the SHG matrix elements. We also speculate that the electronic contribution to the dielectric function and its anisotropy could be quite different for the title compounds and may explain the variance in the PM properties.

 $\text{Cu}_2\text{MnGeS}_4$ surpasses several of the current commercially-available IR-NLO materials in several regards, its sizable $\chi^{(2)}$ value and the greater earth-abundance and the lower HHI values 95 of the elements (production and reserve). In closing, $\text{Cu}_2\text{MnGeS}_4$ may be useful in generating tuneable radiation via wave mixing for low-powered applications in the mid-IR.

Conflicts of interest

There are no conflicts of interest to declare.

Acknowledgements

Authors Aitken, Rondinelli and MacNeil acknowledge support from the United States National Science Foundation under grants DMR-1611198, DMR-2011208 and CHE-1659823, respectively. J.I.J. acknowledges support from the Basic Science Research Programs (2017R1D1A1B03035539 and 2021R1A2C2013625) through the National Research Foundation of Korea (NRF), funded by the Korean government. The authors appreciate G&H Cleveland for supplying the AgGaSe₂ optical-quality crystal reference.

Notes and references

- 1 F. K. Hopkins, Opt. Photonics News, 1998, 9, 32-38.
- R. J. Clewes, C. R. Howle, D. J. M. Stothard, M. H. Dunn,
 G. Robertson, W. Miller, G. Malcolm, G. Maker, R. Cox,
 B. Williams, M. Russel, *Proc. SPIE*, 2012, **8456**, 84560X.
- G. Stoeppler, M. Shellhorn, M. Eichhorn, *Laser Phys.*, 2012, 22, 1095-1098.
- 4 N. Dietz, F. L. Madarasz, *Mat. Sci. Eng.-B-Solid*, 2003, **97**, 182-195.
- D. J. Bamford, D. J. Cook, S. J. Sharpe, A. D. Van Pelt, *Appl. Opt.*, 2007, 46, 3958-3968.
- 6 Petrov, V. Parametric down-conversion devices: The coverage of the mid-infrared spectra range by solidstate laser sources. Opt. Mater., 2012, 34, 536-554.
- J. Hecht, *Laser Focus World*, 2014, **50**, 31-38.
- M. W. Todd, R. A. Provencal, T. G. Owano, B. A. Paldus,
 A. Kachanov, K. I. Vodopyanov, M. Hunter, S. L. Coy, J. I
 Steinfeld, J. T. Arnold, *Appl. Phys. B*, 2002, **75**, 367-376.
- S. Junaid, J Tomko, M. P. Semtsiv, J. Kischkat, W. T. Masselink, C. Pedersen and P. Tidemand-Lichtenberg, Opt. Express, 2018, 26, 2203-2211.
- 10 M. C. Ohmer, R. Pandey, MRS Bull., 1998, 23, 16-22.
- 11 P. G. Schunemann, Proc. SPIE, 2007, 6455, 64550R.
- 12 I. B. Zotova, Y. J. Ding, *Opt. Commun.*, 2001, **198**, 453-
- 13 D. N. Nikogosyan, *Nonlinear Optical Crystals: A Complete Survey*, Springer, New York, NY, 2005.
- 14 A. G. Jackson, M. C. Ohmer, S. R. LeClair, *Infrared Phys. Technol.*, 1997, **38**, 233-244.
- G. D. Boyd, H. M. Kasper, J. H. MacFee, J. Appl. Phys., 1973, 44, 2809-2812.
- Tyazhev, A.; Vedenyapin, V.; Marcbhev, G.; Isaenko, L.; Kolker, D.; Lobanov, S.; Petrov, V.; Yelisseyev, A.; Starikova, M.; Zondy, J.-J. Opt. Mater., 2013, 35, 1612-1615.
- 17 I. Chung, M. G. Kanatzidis, *Chem. Mater.*, 2014, **26**, 849-
- 18 F. Liang, L. Kang, Z. Lin, Y. Wu, *Cryst. Growth Des.*, 2017, **17**, 2254-2289.
- 19 H. Lin, W.-B. Wei, H. Chen, X.-T. Wu, Q.-L. Zhu, Coord. Chem. Rev., 2020, 406, 213150.
- Y. Chi, Z.-D. Sun, Q.-T. Xu, H.-G. Xue, S.-P. Guo, ACS Appl. Mater. Interfaces, 2020, 12, 17699-17705.
- 21 S.-P. Guo, X. Chen, Z.-D. Sun, Y. Chi, B.-W. Liu, X.-M. Jiang, S.-F. Li, H.-G. Xue, S. Deng, V. Duppel, J. Köhler, G.-C. Guo, *Angew. Chem. Int. Ed.*, 2019, **58**, 8087-8091.
- 22 Q.-T. Xi, Z.-D. Sun, Y. Chi, H.-G. Xue, S.-P. Guo, *J. Mater. Chem. C*, 2019, **7**, 11752-11756.
- R.-A. Li, Z. Zhou, Y.-K. Lian, F. Jia, X. Jiang, M.-C. Tang, L.-M. Wu, J. Sun, L. Chen, *Angew Chem. Int. Ed.*, 2020, 59, 11861-11865.

ARTICLE Dalton Transactions

- 24 J. Chen, C. Lin, S. Yang, X. Jiang, S. Shi, Y. Sun, B. Li, S. Fang, N. Ye, Cryst. Growth Des., 2020, 20, 2489-2496.
- 25 Z.-Z. Luo, C.-S. Lin, H.-H. Cui, W.-L. Zhang, H. Zhang, Z.-Z. He, W.-D. Cheng, *Chem. Mater.*, 2014, **26**, 2743-2749.
- 26 J. Yao, D. Mei, L. Bai, Z. Lin, W. Yin, P. Fu, Y. Wu, *Inorg. Chem.*, 2010, 49, 9212-9216.
- 27 S.-F. Li, X.-M. Jiang, B.-W. Liu, D. Yan, H.-Y. Zeng, G.-C. Guo, *Inorg. Chem.*, 2018, **57**, 6783-6786.
- 28 S.-F. Li, X.-M. Jiang, B.-W. Liu, D. Yan, C.-S. Lin, H.-Y. Zeng, G.-C. Guo, Chem. Mater., 2017, 29, 1796-1804.
- 29 B.-W. Liu, X.-M. Jiang, H.-Y. Zeng, G.-C. Guo, *J. Am. Chem. Soc.*, 2020, **142**, 10641-10645.
- 30 H. Lin, H. Chen, Y.-J. Zheng, J.-S. Yu, X.-T. Wu, L.-M. Wu, *Dalton Trans.*, 2017, **46**, 7714-7721.
- 31 Y. Yang, K. Wu, X. Wu, B. Zhang, L. Gao, *J. Mater. Chem. C*, 2020, **8** 1762-1767.
- 32 Y.-J. Lin, B.-W. Liu, R. Ye, X.-M. Jiang, L.-Q. Yang, H.-Y. Zeng, G.-C. Guo, *J. Mater. Chem C*, 2019, **7**, 4459-4465.
- 33 Y.-J. Lin, R. Ye, L.-Q. Yang, X.-M. Jiang, B.-WA. Liu, H.-Y. Zeng, G.-C. Guo, *Inorg. Chem. Front.*, 2019, 6, 2365-2368.
- 34 Y. Pang, A. Zhou, C. Lin, W. Cheng, G.-L. Chai, J. Alloy Compd., 2019, 797, 356-362.
- 35 K. Kato, V. V. Badikov, L. Wang, V. L. Panyutin, K. V. Mitin, K. Miyata, V. Petrov, *Opt. Let.*, 2020, **45**, 2136-2139.
- 36 L.-Q. Yang, R. Ye, X.-M. Jiang, B.-W. Liu, H.-Y. Zeng, G.-C Guo, J. Mater. Chem. C, 2020, 8, 3688-3693.
- 37 A. Zhou, C. Lin, B. Li, W. Cheng, Z. Guo, Z. Hou, F. Yuan, G.-L. Chai, *J. Mater. Chem. C*, 2020, **8**, 7947-7955.
- 38 V. Petrov, V. Badikov, G. Shevyrdyaeva, V. Panyutin, V. Chizhikov, *Opt. Mater.*, 2004, **26**, 217-222.
- 39 Z. Li, S. Zhang, Z. Huang, L.-D. Zhao, E. Uykur, W. Xing, Z. Lin, J. Yao, Y. Wu, Chem. Mater., 2020, 32, 3288-3296.
- J. A. Brant, D. J. Clark, Y. S. Kim, J. I. Jang, A. Weiland, J. A. Aitken, *Inorg. Chem.*, 2015, 54, 2809-2819.
- 41 J.-H. Zhang, D. J. Clark, J. A. Brant, K. A. Rosmus, P. Grima, J. W. Lekse, J. I. Jang and J. A. Aitken, *Chem. Mater.*, 2020, **32**, 8947-8955.
- 42 J. A. Brant, D. J. Clark, Y. S. Kim, J. I. Jang, J.-H. Zhang and J. A. Aitken, *Chem. Mater.* 2014, **26**, 2045-2048.
- 43 J.-H. Zhang, S. S. Stoyko, A. J. Craig, P. Grima, J. W. Kotchey, J. I. Jang and J. A. Aitken, *Chem. Mater.* 2020, 32, 10045-10054.
- 44 K. A. Rosmus, J. A. Brant, S. D. Wisneski, D. J. Clark, Y. S. Kim, J. I. Jang, C. D. Brunetta, J.-H. Zhang, M. N. Srnec, and J. A. Aitken, *Inorg. Chem.*, 2014, **53**, 7809-7811.
- 45 J.-H. Zhang, D. J. Clark, A. Weiland, S.S. Stoyko, Y. S. Kim, J. I. Jang and J. A. Aitken, *Inorg. Chem. Frontier*, 2017, 4, 1472–1484.
- (a) J.-H. Zhang, D. J. Clark, J. A. Brant, C. W. Sinagra, Y. S. Kim, J. I. Jang, and J. A. Aitken, *Dalton Trans*. 2015, 44, 11212-11222. (b) A. Weiland, J.-H. Zhang, D. J. Clark, J. A. Brant, C. W. III Sinagra, Y. S. Kim, J. I. Jang and J. A. Aitken, *Dalton Trans*. 2017, 46, 10102-10104.
- 47 L.-Q. Yang, X.-M. Jiang, G.-C. Guo, *Inorg. Chem. Commun.*, 2020, **115**, 107852.
- 48 G. Li, Y. Chu and Z. Zhou, *Chem. Mater.*, 2018, **30**, 602-606.
- 49 K. Wu, Z. Yang, S. Pan, Chem. Comm., 2017, 53, 3010-3013.
- 50 K. Wu, S. Pan, Crystals, 2017, 7, 107.
- 51 Y. Huang, K. Wu, J. Cheng, Y. Chu, Z. Yang, S. Pan, *Dalton Trans.*, 2019, **48**, 4484-4488.
- 52 G.-M. Li, Y. Chu, J. Li, Z.-X. Zhou, *Dalton Trans.*, 2020, 49, 1975-1980.
- 53 J. Allemand, M. Wintenberger, *Bull. Soc. Fr. Minéral. Cristallogr.*, 1970, **93**, 14-17.

- 54 Y. Shapira, E. J. McNiff Jr, N. F. Oliveira Jr, E. D. Honig, K. Dwight, A. Wold, *Phys. Rev. B*, 1988, **37**, 411-418.
- G. Nenert, T. T. M. Palstra, J. Phys.: Condens. Matter, 2009, 21, 176002.
- N. Sabry, H. Y. Zahran, E. S. Yousef, H. Algarni, A. Umar,
 H. B. Albargi, I. S. Yahia, *Radiat. Phys. Chem.* 2021, 179, 109248.
- 57 M. Beraich, H. Shaili, Z. Hafidi, E. Benhsina, H. Majdoubi, M. Taibi, A. Guenbour, A. Bellauchou, A. Mzerd, F. Bentiss, A. Zarrouk, M. Fahoume, J. Alloy Compd., 2020, 845. 156216.
- 58 Bruker, 2012, APEX2, SMART, SAINT. Bruker AXS Inc., Madison, Wisconsin, USA.
- 59 G. M. Sheldrick, 1996, SADABS. University of Göttingen, Germany.
- G. M. Sheldrick, 2008, XPREP. Bruker AXS Inc., Madison, Wisconsin, USA.
- 61 G. M. Sheldrick, Acta Cryst., 2015, C71, 3-8.
- 62 C. B. Hübschle, G. M. Sheldrick, B. Dittrich, J. Appl. Cryst., 2011, 44, 1281-1284.
- 63 T. Degen, M. Sadki, E. Bron, U. König and G. Nénert, Powder Diffr. 2014, 29, S13-S18.
- 64 J. Faber and T. Fawcett, Acta Cryst. 2002, **B58**, 325-332.
- 65 Kubelka, P. and Munk, F., Z. Technol. Phys. 1931, 12, 593–601.
- 66 R. J. McGowan, Anal. Chem. 1963, 35, 1664-1665.
- 67 G. Kresse, and J. Furthmüller, *Phys. Rev. B*, 1996, **54**, 11169
- 68 G. Kresse, D. Joubert, *Phys. Rev. B*, 1999, **59**, 1758.
- 69 J.P. Perdew, K. Burke and M. Ernzerhof, *Phys. Rev. Lett.*, 1996, **77**, 3865.
- 70 P.E. Blöchl, Phys. Rev. B., 1994, 50, 17953.
- 71 J.P. Perdew, W. Yang, K. Burke, Z. Yang, E.K.U. Gross, M. Scheffler, G.E. Scuseria, T.M. Henderson, I.Y. Zhang, A.Ruzinszky, H. Peng, J. Sun, E. Trushin and A. Görling, PNAS, 2017, 114, 2801-2806.
- 72 J. Heyd, J.E. Peralta, G.E. Scuseria and R.L. Martin, *J. Chem. Phys.*, 2005, **123**, 174101.
- 73 F. P. Bundy and J. S. Kasper, J. Chem. Phys., 1967, 46, 3437-3446.
- 74 C. Frondel and U. B. Marvin, *Nature* 1967, **214**, 587-589.
- 75 T. B. Shiell, D. G. McCulloch, J. E. Bradby, B. Haberl, R. Boehler and D. R. McKenzie, Sci. Rep., 2016, 6, 37232.
- 76 D. Kraus, A. Ravasio, M. Gauthier, D. O. Gericke, J. Vorberger, S. Frydrych, J. Helfrich, L. B. Fletcher, G. Schaumann, B. Nagler, B. Barbrel, B. Bachmann, E. J. Gamboa, S. Göde, E. Granados, G. Gregori, H. J. Lee, P. Neumayer, W. Schumaker, T. Döppner, R. W. Falcone, S. H. Glenzer and M. Roth, *Nature Commun.*, 2016, 7, 10970.
- 77 A. Lafond, L. Choubrac, C. Guillot-Deudon, P. Deniard, S. Jobic, *Z. Anorg. Allg. Chem.*, 2012, **638**, 2572-2577.
- 78 S. Schorr, Sol. Energy Mater. Sol. Cells, 2011, **95**, 1482-
- 79 G. Gurieva, D. M. Többens, M. Ya. Valakh, S. Schorr, J. Phys. Chem. Sol., 2016, 99, 100-104.
- 80 L. Pauling, J. Am. Chem. Soc. 1929, 51, 1010-1026.
- C. D. Brunetta, J. A. Brant, K. A. Rosmus, K. M. Henline,
 E. Karey, J. H. MacNeil, J. A. Aitken, J. Alloy Compd.,
 2013, 574, 495-503.
- 82 C. W. Sinagra III, F. O. Saouma, C. O. Otieno, S. H. Lapidus, J.-H. Zhang, A. J. Craig, P. Grima-Gallardo, J. A. Brant, K. A. Rosmus, K. E. Rosello, J. I. Jang, J. A. Aitken, *J. Alloy Compd.*, 2021, submitted.
- 83 J. George, D. Waroquiers, D. Di Stefano, G. Petretto, G.-M. Rignanese, G. Hautier, *Angew. Chem. Int. Ed.*, 2020, 59, 7569-7575.

Dalton Transactions ARTICLE

- 84 I. D. Brown, The Chemical Bond in Inorganic Chemistry: The Bond Valence Model, Second Edition, Oxford University Press, Oxford, United Kingdom 2016.
- 85 I. D. Brown, *Z. Kristallog.*, 1992, **199**, 255-272.
- 86 I. D. Brown, D. Altermatt, Acta. Cryst., 1985, **B41**, 244-247.
- T. Bernert, A. Pfitzner, Z. Kristallogr., 2005, 220, 968-972.
- 88 W. Schäfer, R. Nitsche, *Z. Kristallogr.* 1977, **145**, 356-370
- 89 F. Urbach, Phys. Rev., 1953, 92, 1324.
- 90 M. Chourio, H. Romero, L. Betancourt, V. Sagredo, Crystal growth and magnetic properties of the Cu₂MnGeS₄ semiconductor in New Trends in Magnetism, Magnetic Materials, and Their Applications, Plenum Press, New York, 1994, pg 359-363.
- 91 S.K. Kurtz, T. T. Perry, J. Appl. Phys., 1968, **39**, 3798.
- 92 A. G. Jackson, M. C. Ohmer, S. R. LeClair, *Infrared Phys. Technol.* 1997, **38**, 233-244.
- 93 F. O. Saouma, C. C. Stoumpos, J. Wong, M. G. Kanatzidis, J. I. Jang, *Nature Commun.*, 2017, **8**, 742.
- 94 M. Sheik-Bahae, D. C. Hutchings, D. Hagan, E. W. van Stryland, *IEEE J. Quantum Electron.*, 1991, **27**, 1296-1309.
- 95 M. W. Gaultois, T. D. Sparks, C. K. H. Borg, R. Seshadri, W. D. Bonificio, D. R. Clarke, *Chem. Mater.*, 2013, 25, 2911-2920.

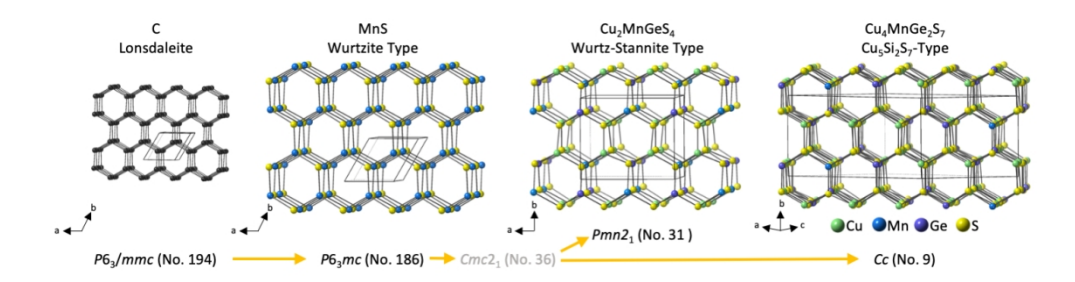


Figure 1. Derivation of the structures of Cu_2MnGeS_4 and $Cu_4MnGe_2S_7$ from wurtzite-type MnS and hexagonal diamond, i.e. Lonsdaleite, via group-subgroup relationships of space groups.

177x46mm (209 x 209 DPI)

Dalton Transactions Page 14 of 34

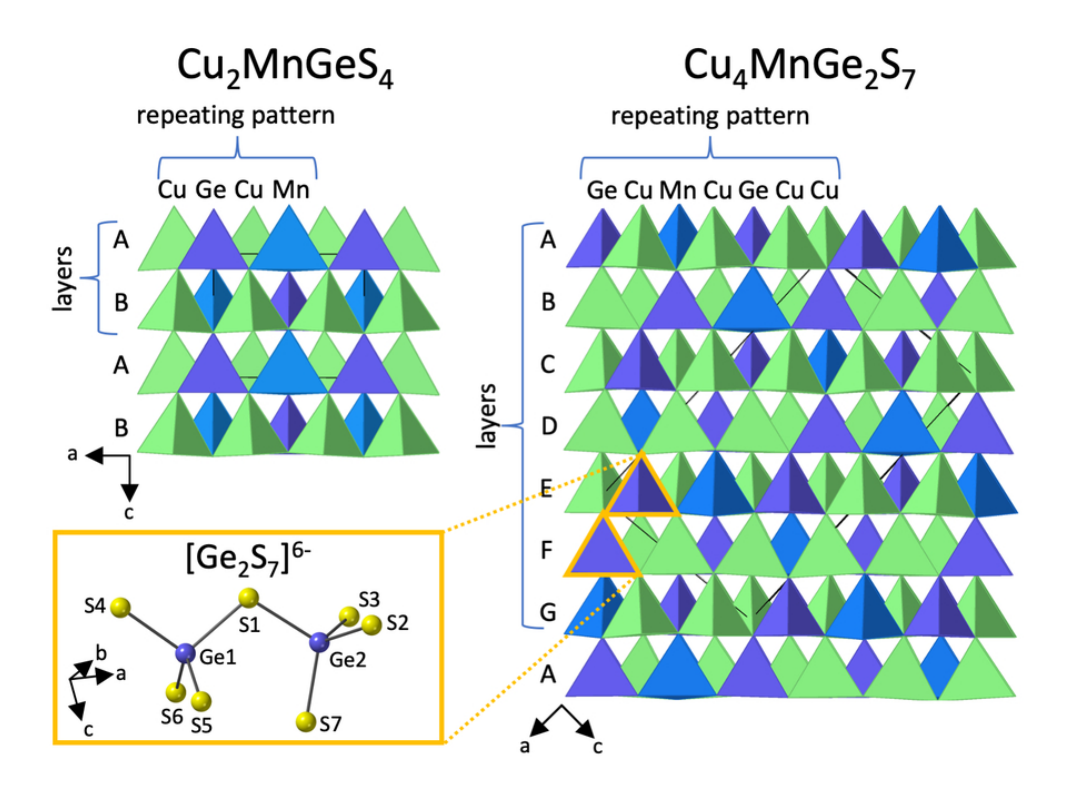


Figure 2. Polyhedral representation of Cu_2MnGeS_4 and $Cu_4MnGe_2S_7$ viewed down the crystallographic b-axes. Copper-, manganese- and germanium-centred tetrahedra are shown in green, blue and purple, respectively. The lack of an inversion centre is obvious, as all the tetrahedral units are uniformly pointing in the same direction. The $[Ge_2S_7]^{6-}$ moiety, present in only $Cu_4MnGe_2S_7$, is enlarged.

76x57mm (300 x 300 DPI)

Page 15 of 34

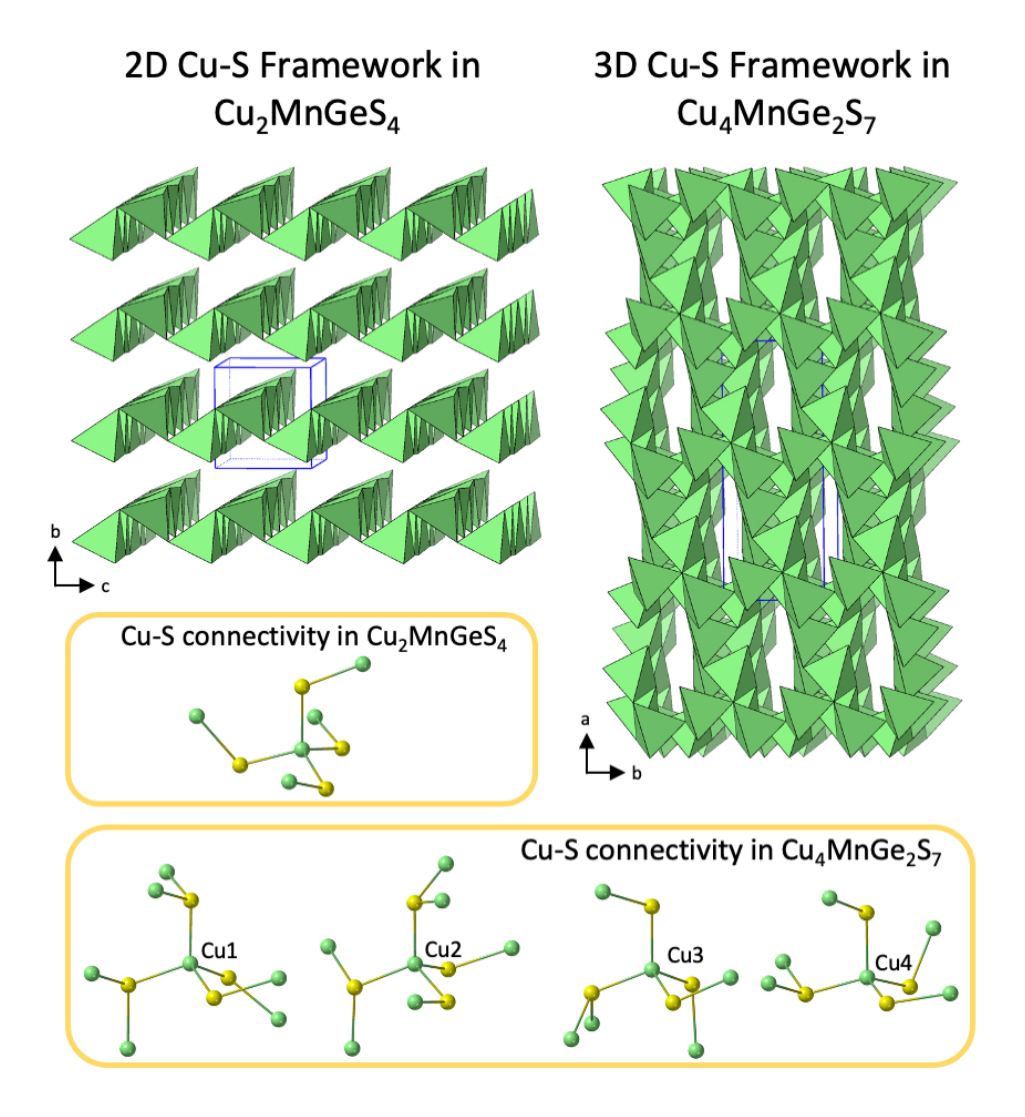


Figure 3 The structures of Cu_2MnGeS_4 and $Cu_4MnGe_2S_7$ with manganese and germanium atoms omitted are presented on top. The different connectivity of the crystallographically unique CuS_4 tetrahedra in each structure is highlighted in yellow.

88x93mm (258 x 258 DPI)

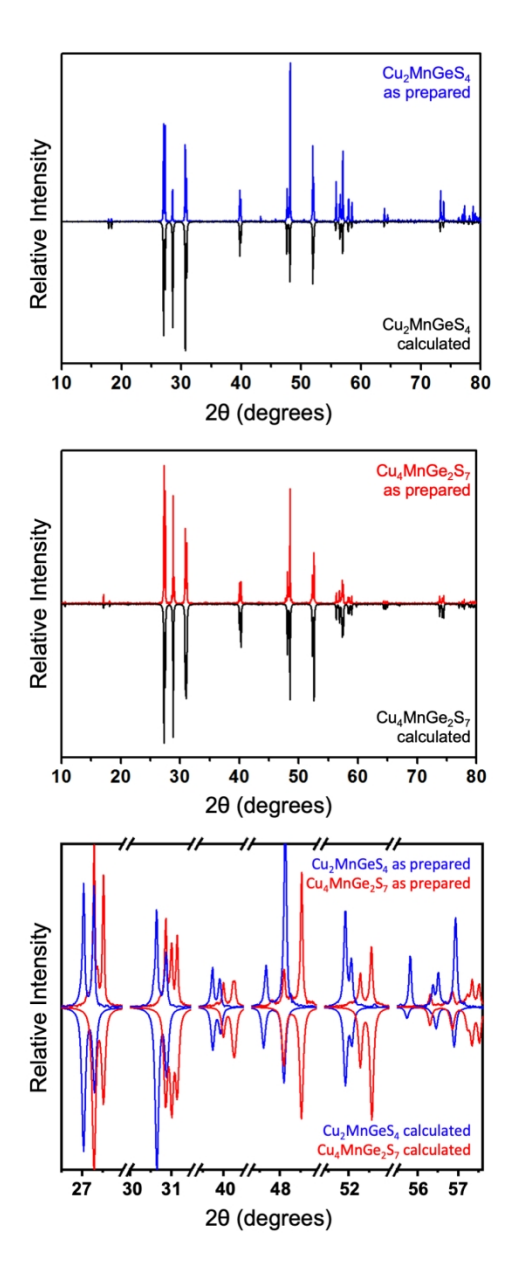


Figure 4. X-ray powder diffraction patterns for Cu_2MnGeS_4 (top) and $Cu_4MnGe_2S_7$ (middle) compared to those calculated from the single crystal X-ray structures. Blown-up selected regions of the two experimental patterns compared to the corresponding calculated patterns (bottom) clearly show that the two phases were prepared nearly phase pure, i.e. single phase.

83x207mm (275 x 275 DPI)

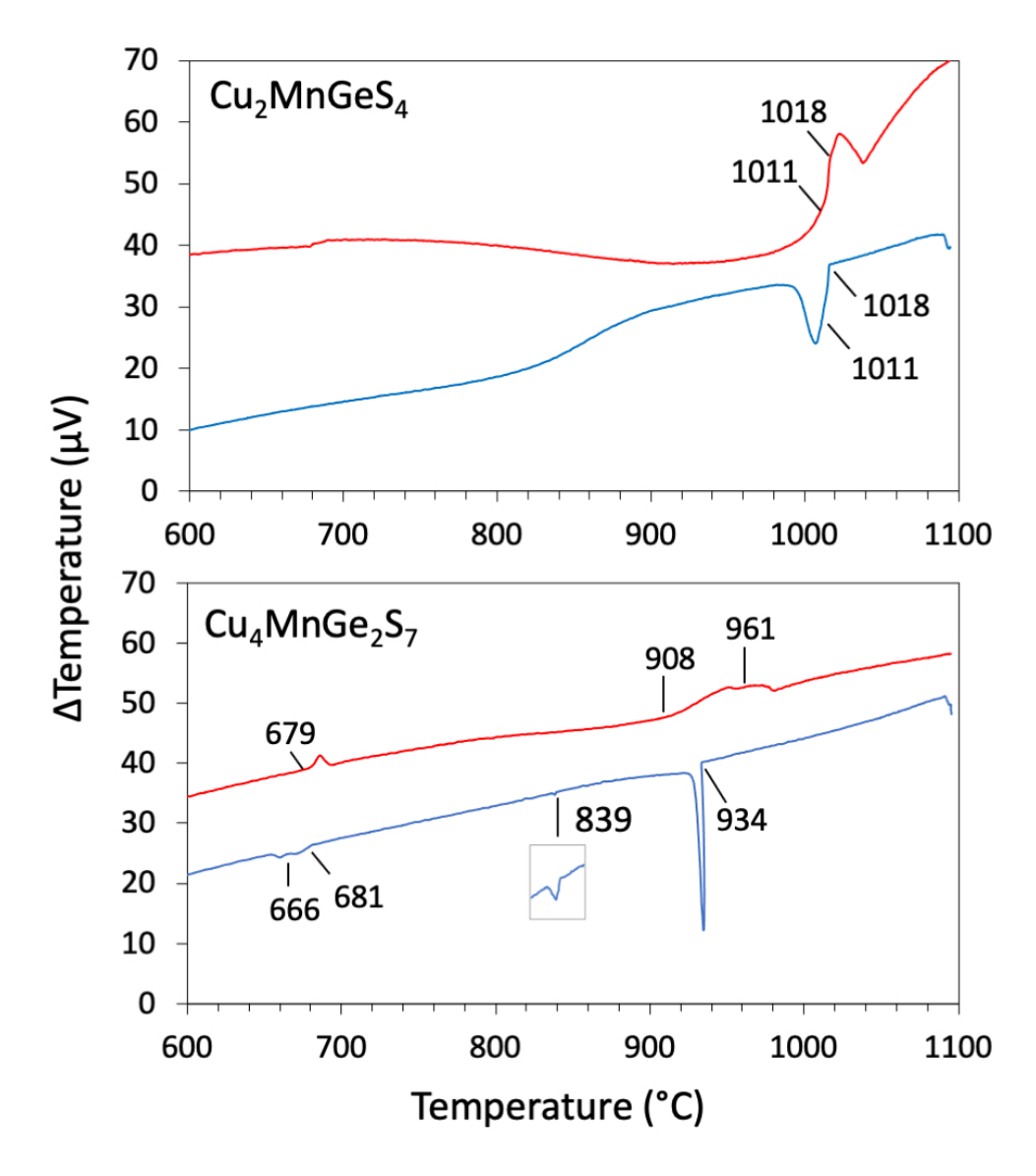


Figure 5 Differential thermal analysis curves for Cu_2MnGeS_4 (cycle 1) and $Cu_4MnGe_2S_7$ (cycle 2). Heating and cooling curves are displayed in red and blue, respectively.

163x184mm (143 x 143 DPI)

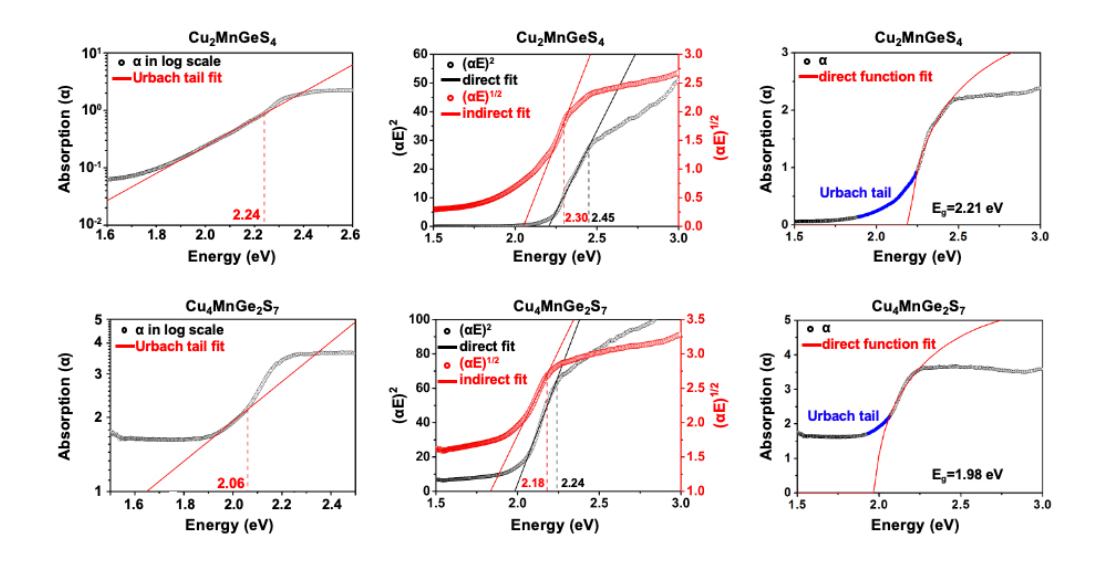


Figure 6. UV/vis/NIR optical diffuse reflectance data converted to absorption for Cu_2MnGeS_4 (top) and $Cu_4MnGe_2S_7$ (bottom). Left: The log of the absorption as a function of energy was plotted and used to pinpoint the Urbach tail. The high-energy end of the tail region is labelled in red. Middle: The square and square root of the absorption as a function of energy were plotted to accentuated direct and indirect bandgap transitions, respectively. The high energy side of the linear regions are labelled in black and red for the direct and indirect fits, respectively. Right: The bandgap values were obtained by fitting the absorption edge data to the function for direct-bandgap semiconductors.

177x95mm (129 x 129 DPI)

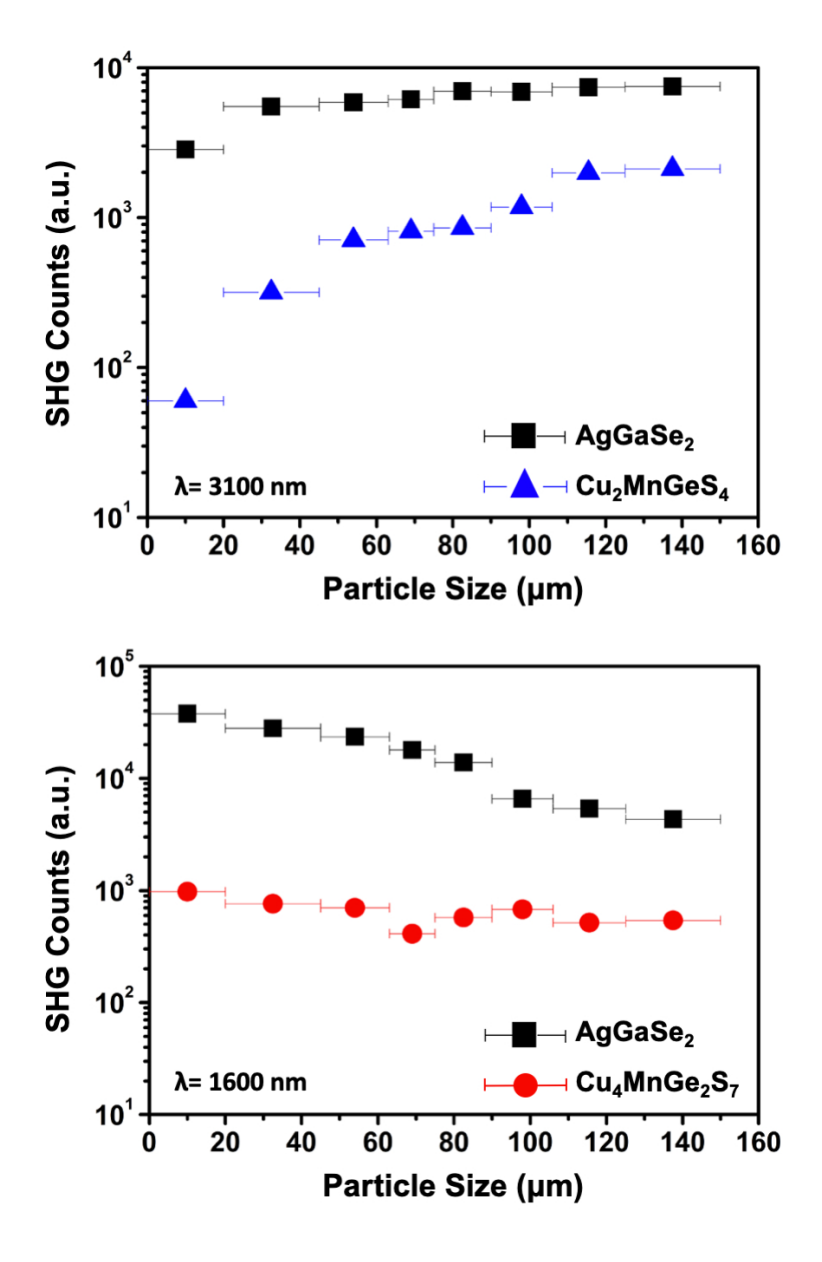


Figure 7. Measured SHG response as function of particle size range for Cu_2MnGeS_4 (top) at $\lambda=3100$ nm and $Cu_4MnGe_2S_7$ (bottom) at $\lambda=1600$ nm, compared to the reference.

79x121mm (289 x 289 DPI)

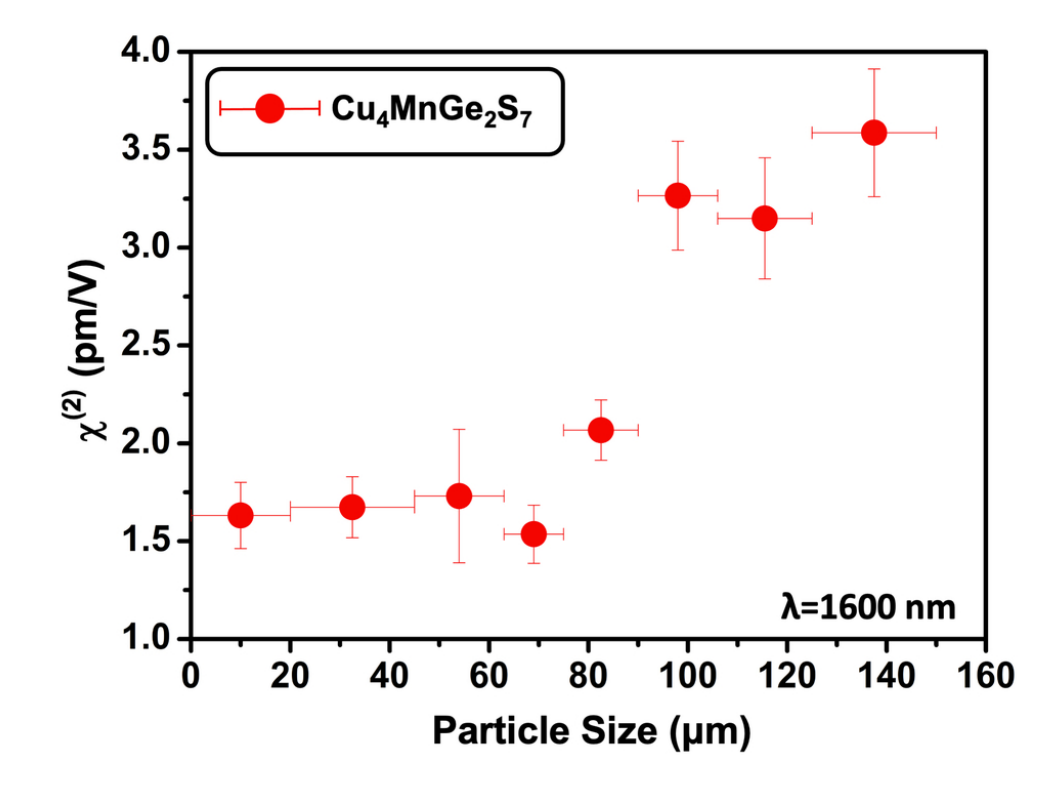


Figure 8. The $\chi^{(2)}$ values as a function of particle size range for Cu₄MnGe₂S₇ measured at λ =1600 nm. The $\chi^{(2)}$ values were computed using equation 4.

82x61mm (300 x 300 DPI)

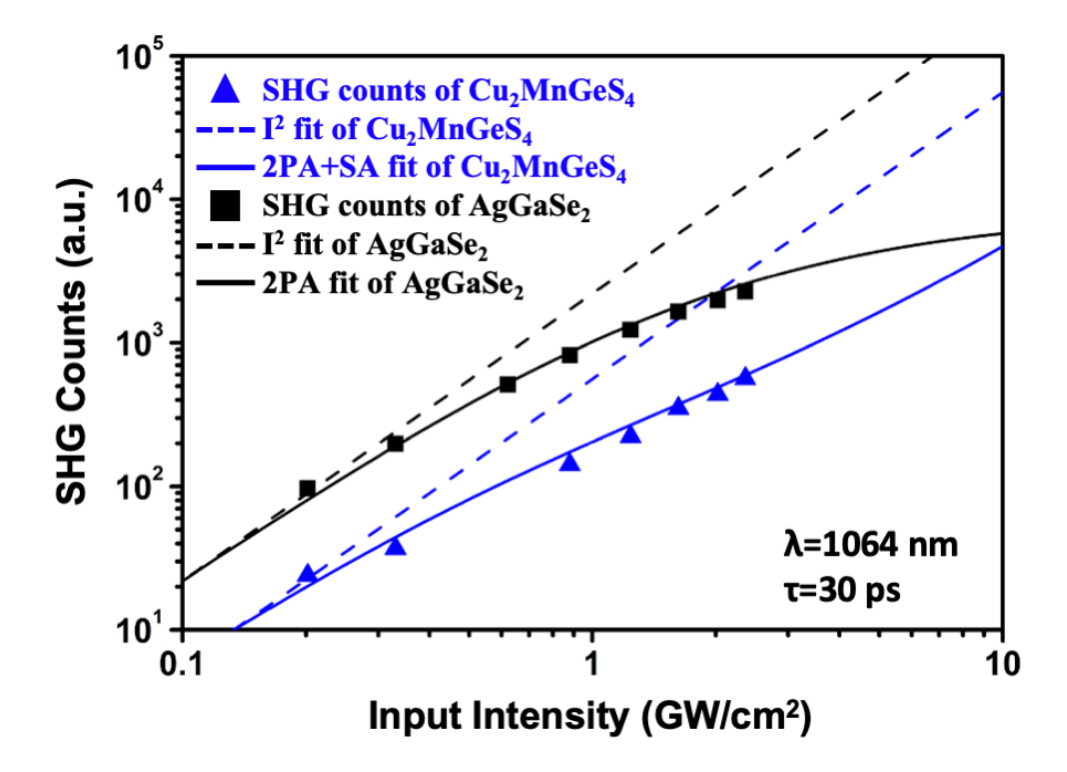


Figure 9. SHG response as a function of input laser intensity for Cu_2MnGeS_4 (blue) compared to that of an optical-quality $AgGaSe_2$ reference material (black). The wavelength and the pulse width were 1064 nm and 30 ps, respectively for these measurements.

82x61mm (278 x 278 DPI)

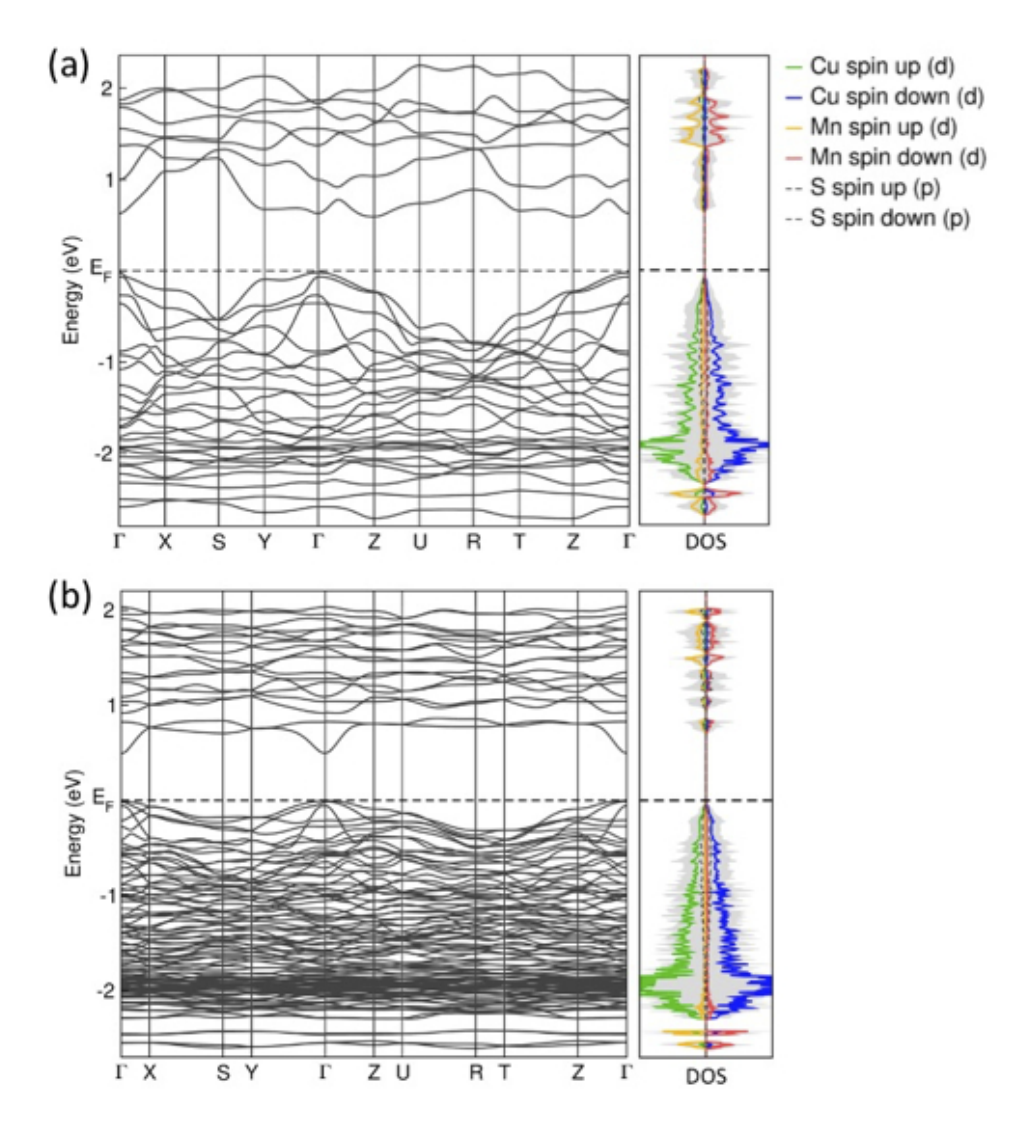


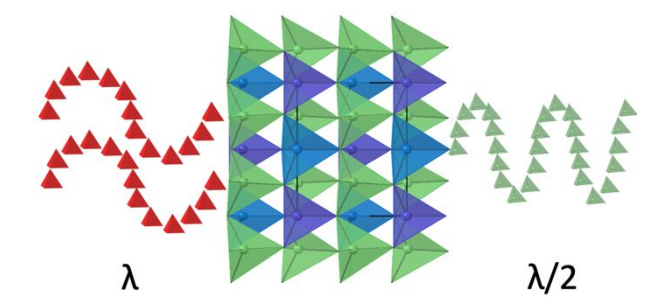
Figure 10. The electronic band structure and projected DOS of (a) Cu_2MnGeS_4 (b) $Cu_4MnGe_2S_7$, at the DFT-PBE level. The shaded areas in the DOS plot are the total DOS and the coloured lines represent the projected DOS. The contribution from Ge is significantly smaller than the other atomic species within this energy window and is therefore not shown.

87x92mm (150 x 150 DPI)

 $Cu_4MnGe_2S_7$ and Cu_2MnGeS_4 : Two Polar Thiogermanates Exhibiting Second Harmonic Generation in the Infrared and Structures Derived from Hexagonal Diamond.

Table of Contents Entry

The synthesis, structure, and physicochemical characterization of two diamond-like semiconductors are reported. Both compounds display second harmonic generation, bandgaps around 2 eV and wide windows of optical transparency in the infrared.



Cu₂MnGeS₄ and Cu₄MnGe₂S₇: Two Polar Thiogermanates Exhibiting Second Harmonic Generation in the Infrared and Structures Derived from Hexagonal Diamond.

Jennifer R. Glenn,^a Jeong Bin Cho,^b Yiqun Wang,^c Andrew J. Craig,^a Jian-Han Zhang,^d Marvene Cribbs,^a Stanislav S. Stoyko,^a Christopher Barton,^a Allyson Bonnoni,^a Kate E. Rosello,^a Pedro Grima-Gallardo,^{e,f} Joseph H. MacNeil,^g James M. Rondinelli,^c Joon I. Jang,^b and Jennifer A. Aitken^a

Supporting Information

Item	Page
Table S1. Crystal data, data collection and structure refinement details for Cu ₄ MnGe ₂ S ₇ .	S2
Table S2. Fractional atomic coordinates and isotropic or equivalent isotropic displacement parameters (Ų) for Cu₄MnGe₂S ₇ .	S3
Table S3. Atomic displacement parameters (Ų) for Cu₄MnGe₂S7.	S3
Table S4. Bond distances (Å) for Cu₄MnGe₂S ₇ .	S4
Table S5. Bond angles (°) for Cu₄MnGe₂S ₇ .	S5
Table S6. Average bond distances (Å) and angles (°) for Cu₄MnGe₂S ₇ .	S6
Table S7. Extended connectivity table for $Cu_4MnGe_2S_7$ used to predict structural distortions according to Pauling's second rule.	S7
Table S8. Bond valence sums, provided for each crystallographically unique ion, and global instability index (G) values for Cu₂MnGeS₄ and Cu₄MnGe₂S₃.	S8
Table S9. The electronic bandgaps at different k -points using the PBE and HSE06 functional in Cu_2MnGeS_4 .	S9
Table S10: The electronic bandgaps at different k -points using the PBE and HSE06 functional in $Cu_4MnGe_2S_7$.	S9
Figure S1. Simulated precession images for Cu₄MnGe₂S ₇ created using the single-crystal X-ray diffraction data. The (0kl), (h0l), and (hk0) planes in reciprocal space are shown from left to right, respectively. Sharp, bright spots are observed indicative of a single crystal.	S10
Figure S2. Differential thermal analysis diagrams for Cu ₂ MnGeS ₄ (top) and Cu ₄ MnGe ₂ S ₇ (bottom). Two cycles were conducted for each experiment.	S11
Figure S3. Attenuated total reflectance FT-IR data converted to transmittance for Cu₂MnGeS₄ and Cu₄MnGe₂S ₇ .	S11

Table S1. Crystal data, data collection and structure refinement details for Cu₄MnGe₂S₇.

Formula weight	678.70
Crystal system, space group	Monoclinic, Cc (No.9)
Temperature (K)	296
α (Å)	16.7332(3)
b (Å)	6.47600(10)
c (Å)	9.8022(2)
β(°)	93.1517(9)
V (Å ³)	1060.60(3)
Z	4
F(000)	1268
Density g cm ⁻³	4.250
Radiation type	Mo Ka
μ (mm ⁻¹)	15.93
Crystal size (mm)	0.18 x 0.14 x 0.10
Crystal habit and color	Irregular polyhedron, black
Diffractometer	Bruker SMART Apex II
Radiation source	Fine-focus sealed tube
Absorption correction	Multi-scan, SADABS (Sheldrick, 2002)
No. of measured reflections	4396
No. of independent reflections	2405
No. of observed reflections [$I > 2\sigma(I)$]	2282
θ_{min} , θ_{max} (°)	2.4, 27.5
Completeness to θ =27.5°	100%
	$-21 \le h \le 21$
Limiting indices	-8 ≤ <i>k</i> ≤ 8
	-12 ≤ <i>l</i> ≤ 12
R _{int}	0.015
$R[F^2 > 2\sigma(F^2)], wR(F^2), S$	0.021, 0.055, 1.07
(Δ/σ) _{max}	0.001
Extinction coefficient	0.00567 (18)
No. of data/restraints/parameters	0.70
$\Delta \rho_{\text{max}}$, $\Delta \rho_{\text{min}}$ (e Å ⁻³)	-0.89
Absolute structure parameter (Flack parameter)	0.063 (12)

Table S2. Fractional atomic coordinates and isotropic or equivalent isotropic displacement parameters (\mathring{A}^2) for $Cu_4MnGe_2S_7$.

	x	у	Z	$U_{ m iso}*/U_{ m eq}$
Cu1	-0.00193 (6)	0.18000 (17)	-0.00131 (13)	0.0196 (3)
Cu2	0.06549 (5)	0.3393 (2)	0.36035 (14)	0.0190(2)
Cu3	0.21237 (5)	0.3196 (2)	0.07988 (12)	0.0197 (3)
Cu4	0.35325 (4)	0.67831 (12)	0.28351 (9)	0.0186 (3)
Mn	0.28394 (8)	0.15156 (18)	0.43729 (12)	0.0143 (2)
Ge1	0.42802(3)	0.16344 (7)	0.15672 (6)	0.00867 (19)
Ge2	0.63880 (4)	0.32497 (18)	0.22799 (10)	0.00879 (19)
S1	0.03322 (11)	0.16743 (19)	0.56571 (13)	0.0090(3)
S2	0.17008 (10)	0.15178 (17)	0.27258 (13)	0.0118 (4)
S3	0.24068 (10)	0.6649 (2)	0.13736 (14)	0.0120 (4)
S4	0.32846 (10)	0.19229 (18)	-0.00212 (15)	0.0108 (3)
S5	0.39302 (10)	0.33995 (19)	0.33827 (13)	0.0107(3)
S6	0.46156 (9)	0.16029 (18)	0.69731 (14)	0.0099 (4)
S7	0.60848 (10)	0.1666 (2)	0.41601 (15)	0.0106(3)

Table S3. Atomic displacement parameters (\mathring{A}^2) for $Cu_4MnGe_2S_7$.

	U^{11}	U^{22}	U^{33}	U^{12}	U^{13}	U^{23}
Cu1	0.0179 (4)	0.0244 (4)	0.0164 (5)	-0.0028 (4)	0.0016 (3)	-0.0014 (3)
Cu2	0.0189 (5)	0.0167 (4)	0.0211 (4)	-0.0003(3)	-0.0021(3)	-0.0012(3)
Cu3	0.0168 (5)	0.0216 (5)	0.0205 (5)	0.0016(3)	-0.0001 (4)	-0.0003(3)
Cu4	0.0183 (5)	0.0191 (4)	0.0186 (6)	-0.0008(4)	0.0022 (4)	-0.0004(3)
Mn	0.0127 (4)	0.0157 (4)	0.0144 (5)	0.0003 (5)	0.0006 (4)	-0.0003 (4)
Ge1	0.0075(3)	0.0090(3)	0.0094(3)	0.0002(3)	0.0000(2)	-0.0009(2)
Ge2	0.0086(3)	0.0080(2)	0.0096 (4)	0.0002(2)	-0.0006 (2)	0.00001 (19)
S1	0.0076 (6)	0.0094 (5)	0.0100(6)	0.0004 (5)	0.0008 (5)	-0.0012 (4)
S2	0.0140 (9)	0.0081 (6)	0.0132 (7)	-0.0005(5)	0.0004 (6)	-0.0006 (4)
S3	0.0119 (10)	0.0111 (6)	0.0130 (6)	0.0017 (4)	0.0010(6)	-0.0006 (4)
S4	0.0078 (8)	0.0140 (5)	0.0104 (5)	-0.0003(5)	-0.0005(5)	0.0018 (5)
S5	0.0115 (8)	0.0104 (6)	0.0102 (6)	0.0012 (4)	0.0020 (6)	-0.0016 (4)
S6	0.0104 (9)	0.0087 (5)	0.0108 (6)	-0.0007 (4)	0.0020 (6)	-0.0002 (4)
S7	0.0124 (9)	0.0101(6)	0.0095 (5)	0.0002 (5)	0.0012 (6)	0.0011 (4)

Table S4. Bond distances (Å) for Cu₄MnGe₂S₇.

Cu1—S7 ⁱ	2.2852 (18)	Cu4—S4 ^v	2.321 (2)
Cu1—S5i	2.2969 (17)	Cu4—S5	2.3437 (16)
Cu1—S6i	2.3161 (18)	Mn — $S4^{vi}$	2.4119 (17)
Cu1—S1 ⁱⁱ	2.4077 (14)	Mn—S2	2.429 (2)
Cu2—S7 ⁱⁱⁱ	2.2942 (15)	Mn—S3 ^v	2.4371 (18)
Cu2—S6 ⁱ	2.2963 (16)	Mn—S5	2.441 (2)
Cu2—S2	2.3332 (19)	Ge1—S6 ⁱⁱ	2.2008 (13)
Cu2—S1	2.3879 (17)	Ge1—S5	2.2207 (14)
Cu3—S4	2.2959 (17)	Ge1—S4	2.2247 (15)
Cu3—S7 ⁱ	2.3029 (16)	Ge1—S1 ^{vii}	2.2949 (16)
Cu3—S2	2.3230 (18)	Ge2—S7	2.1930 (14)
Cu3—S3	2.348 (2)	Ge2—S2viii	2.2179 (15)
Cu4—S6 ^{iv}	2.2933 (18)	Ge2—S3 ^{ix}	2.2218 (16)
Cu4—S3	2.3046 (16)	Ge2—S1 ^{vii}	2.3120 (15)

Symmetry codes: (i) x-1/2, -y+1/2, z-1/2; (ii) x, -y, z-1/2; (iii) x-1/2, y+1/2, z; (iv) x, -y+1, z-1/2; (v) x, -y+1, z+1/2; (vi) x, -y, z+1/2; (vii) x+1/2, y+1/2, z; (ix) x+1/2, z; (ix) x+1/2,

Table S5. Bond angles (°) for Cu₄MnGe₂S₇.

S7 -Cu -S6 112.64 (8)				
$\begin{array}{cccccccccccccccccccccccccccccccccccc$	S7 ⁱ —Cu1—S5 ⁱ	112.64 (8)	Ge1 ^x —S1—Ge2 ^x	107.21 (6)
$\begin{array}{c ccccccccccccccccccccccccccccccccccc$	S7 ⁱ —Cu1—S6 ⁱ	` '	Ge1 ^x —S1—Cu2	` /
$\begin{array}{cccccccccccccccccccccccccccccccccccc$	S5 ⁱ —Cu1—S6 ⁱ	, ,	Ge2x—S1—Cu2	` '
$\begin{array}{c ccccccccccccccccccccccccccccccccccc$	S7 ⁱ —Cu1—S1 ⁱⁱ		Ge1 ^x —S1—Cu1 ^{vi}	· /
$\begin{array}{c ccccccccccccccccccccccccccccccccccc$	S5 ⁱ —Cu1—S1 ⁱⁱ	` '	Ge2 ^x —S1—Cu1 ^{vi}	` '
$\begin{array}{c ccccccccccccccccccccccccccccccccccc$	S6 ⁱ —Cu1—S1 ⁱⁱ	105.05 (8)	Cu2—S1—Cu1 ^{vi}	105.59 (7)
$\begin{array}{c ccccccccccccccccccccccccccccccccccc$	S7 ⁱⁱⁱ —Cu2—S6 ⁱ	` '	Ge2 ^{xi} —S2—Cu3	` '
$\begin{array}{c ccccccccccccccccccccccccccccccccccc$	S7 ⁱⁱⁱ —Cu2—S2	` '	Ge2 ^{xi} —S2—Cu2	
$\begin{array}{c ccccccccccccccccccccccccccccccccccc$	S6 ⁱ —Cu2—S2	` '	Cu3—S2—Cu2	` '
$\begin{array}{cccccccccccccccccccccccccccccccccccc$	S7 ⁱⁱⁱ —Cu2—S1	. ,	Ge2 ^{xi} —S2—Mn	` '
$\begin{array}{cccccccccccccccccccccccccccccccccccc$	S6 ⁱ —Cu2—S1	112.92 (7)	Cu3—S2—Mn	106.14 (9)
$\begin{array}{c ccccccccccccccccccccccccccccccccccc$	S2—Cu2—S1	` '	Cu2—S2—Mn	` '
$\begin{array}{cccccccccccccccccccccccccccccccccccc$	S4—Cu3—S7 ⁱ	112.99 (9)	Ge2 ⁱⁱⁱ —S3—Cu4	110.65 (7)
$\begin{array}{c ccccccccccccccccccccccccccccccccccc$	S4—Cu3—S2	` '	Ge2 ⁱⁱⁱ —S3—Cu3	
$\begin{array}{cccccccccccccccccccccccccccccccccccc$	S7 ⁱ —Cu3—S2		Cu4—S3—Cu3	
$\begin{array}{cccccccccccccccccccccccccccccccccccc$	S4—Cu3—S3	* /	Ge2 ⁱⁱⁱ —S3—Mn ^{iv}	* *
$\begin{array}{cccccccccccccccccccccccccccccccccccc$	S7 ⁱ —Cu3—S3	()	Cu4—S3—Mn ^{iv}	
$\begin{array}{c ccccccccccccccccccccccccccccccccccc$	S2—Cu3—S3		Cu3—S3—Mn ^{iv}	
$\begin{array}{cccccccccccccccccccccccccccccccccccc$	S6iv—Cu4—S3		Ge1—S4—Cu3	` ′
$\begin{array}{cccccccccccccccccccccccccccccccccccc$		` ′		· /
$\begin{array}{c ccccccccccccccccccccccccccccccccccc$	S3—Cu4—S4 ^v	` '	Cu3—S4—Cu4 ^{iv}	` '
$\begin{array}{cccccccccccccccccccccccccccccccccccc$	S6 ^{iv} —Cu4—S5	106.88 (6)	Ge1—S4—Mn ⁱⁱ	` ′
$\begin{array}{cccccccccccccccccccccccccccccccccccc$	S3—Cu4—S5	` '	Cu3—S4—Mn ⁱⁱ	` /
$\begin{array}{cccccccccccccccccccccccccccccccccccc$	S4 ^v —Cu4—S5		$Cu4^{iv}$ — $S4$ — Mn^{ii}	` /
$\begin{array}{cccccccccccccccccccccccccccccccccccc$	S4 ^{vi} —Mn—S2	112.62 (7)	Ge1—S5—Cu1 ^{xii}	107.10 (8)
$\begin{array}{cccccccccccccccccccccccccccccccccccc$	$S4^{vi}$ — Mn — $S3^{v}$		Ge1—S5—Cu4	
$\begin{array}{cccccccccccccccccccccccccccccccccccc$	S2—Mn—S3 ^v	106.13 (7)	Cu1 ^{xii} —S5—Cu4	113.98 (6)
$\begin{array}{cccccccccccccccccccccccccccccccccccc$	S4 ^{vi} —Mn—S5		Ge1—S5—Mn	107.30 (5)
$\begin{array}{cccccccccccccccccccccccccccccccccccc$	S2—Mn—S5	108.17 (7)	Cu1 ^{xii} —S5—Mn	105.10 (6)
$\begin{array}{cccccccccccccccccccccccccccccccccccc$	S3 ^v —Mn—S5	, ,		
$\begin{array}{cccccccccccccccccccccccccccccccccccc$	S6 ⁱⁱ —Ge1—S5	114.92 (6)	Ge1 ^{vi} —S6—Cu4 ^v	107.58 (7)
$\begin{array}{cccccccccccccccccccccccccccccccccccc$	S6 ⁱⁱ —Ge1—S4		Ge1 ^{vi} —S6—Cu2 ^{xii}	
$\begin{array}{cccccccccccccccccccccccccccccccccccc$	S5—Ge1—S4	107.29 (6)	Cu4 ^v —S6—Cu2 ^{xii}	
$\begin{array}{cccccccccccccccccccccccccccccccccccc$	S6 ⁱⁱ —Ge1—S1 ^{vii}	` '	Ge1 ^{vi} —S6—Cu1 ^{xii}	110.48 (7)
$\begin{array}{cccccccccccccccccccccccccccccccccccc$		107.92 (5)	Cu4 ^v —S6—Cu1 ^{xii}	110.89 (6)
$\begin{array}{cccccccccccccccccccccccccccccccccccc$	S4—Ge1—S1 ^{vii}	104.40 (6)	Cu2 ^{xii} —S6—Cu1 ^{xii}	, ,
$\begin{array}{cccccccccccccccccccccccccccccccccccc$	S7—Ge2—S2 ^{viii}	* *		, ,
$\begin{array}{cccccccccccccccccccccccccccccccccccc$	S7—Ge2—S3 ^{ix}	109.62 (6)	Ge2—S7—Cu2 ^{ix}	108.44 (8)
$S2^{viii}$ — $Ge2$ — $S1^{vii}$ 106.16 (6) $Cu1^{xii}$ — $S7$ — $Cu3^{xii}$ 109.25 (7)	S2viii—Ge2—S3ix	, ,	$Cu1^{xii}$ —S7— $Cu2^{ix}$, ,
$S2^{viii}$ — $Ge2$ — $S1^{vii}$ 106.16 (6) $Cu1^{xii}$ — $S7$ — $Cu3^{xii}$ 109.25 (7)	S7—Ge2—S1 ^{vii}	112.63 (8)	Ge2—S7—Cu3 ^{xii}	111.55 (12)
$S3^{ix}$ — $Ge2$ — $S1^{vii}$ 108.00 (8) $Cu2^{ix}$ — $S7$ — $Cu3^{xii}$ 114.62 (7)	S2 ^{viii} —Ge2—S1 ^{vii}	` '	Cu1 ^{xii} —S7—Cu3 ^{xii}	` '
	S3 ^{ix} —Ge2—S1 ^{vii}	108.00 (8)	$Cu2^{ix}$ — $S7$ — $Cu3^{xii}$	114.62 (7)

Symmetry codes: (i) x-1/2, -y+1/2, z-1/2; (ii) x, -y, z-1/2; (iii) x-1/2, y+1/2, z; (iv) x, -y+1, z-1/2; (v) x, -y+1, z+1/2; (vi) x, -y, z+1/2; (vii) x+1/2, y+1/2, z+1/2; (viii) x+1/2, y+1/2, z; (ix) x+1/2, z; (ix) x+

Table S6. Average bond distances (Å) and angles (°) for Cu₄MnGe₂S₇.

-	Average bond distance (Å)	Average bond angle (°)
Cu1-S	2.326(3)	S-Cu1-S 109.4(2)
Cu2-S	2.328(3)	S-Cu2-S 109.4(2)
Cu3-S	2.317(4)	S-Cu3-S 109.4(2)
Cu4-S	2.316(4)	S-Cu4-S 109.3(2)
All Cu-S	2.322(7)	S-Ge1-S 109.4(1)
Ge1-S	2.235(3)	S-Ge2-S 109.5(2)
Ge2-S	2.236(3)	S-Mn-S 109.5(2)
All Ge-S	2.236(4)	All S-Cu-S 109.4(3)
Ge-S (short)*	2.213(4)	All S-Ge-S 109.4(2)
Mn-S	2.430(4)	S-Cu1-S 109.4(2)
S1-M	2.351(3)	
S2-M	2.326(4)	
S3-M	2.328(4)	
S4-M	2.313(3)	
S5-M	2.326(3)	
S6-M	2.277(3)	
S7-M	2.269(3)	
All S-M	2.313(9)	

^{*}The short Ge-S bond average excludes the Ge1-S1 and Ge2-S1 bonds.

Table S7. Extended connectivity table for $Cu_4MnGe_2S_7$ used to predict structural distortions according to Pauling's second rule. When the charge on the sulfur is compensated (CMP) by the cations in its first coordination sphere the coordination polyhedron is regular. When the charge of the sulfur is over CMP or under CMP cation-anion bonds will lengthen and shorten, respectively.

	Anions								Horizontal Bond Strength
		S1	S2	S3	S4	S5	S6	S 7	Sums
	Cu1	$\frac{1}{4}$				$\frac{1}{4}$	$\frac{1}{4}$	$\frac{1}{4}$	Σ = 1
	Cu2	$\frac{1}{4}$	$\frac{1}{4}$				$\frac{1}{4}$	$\frac{1}{4}$	Σ = 1
Cations	Cu3		$\frac{1}{4}$	$\frac{1}{4}$	$\frac{1}{4}$			$\frac{1}{4}$	$\Sigma = 1$
	Cu4			$\frac{1}{4}$	$\frac{1}{4}$	$\frac{1}{4}$	$\frac{1}{4}$		$\Sigma = 1$
	Mn		$\frac{2}{4}$	$\frac{2}{4}$	$\frac{2}{4}$	$\frac{2}{4}$			$\Sigma = 2$
	Ge1	$\frac{4}{4}$			$\frac{4}{4}$	$\frac{4}{4}$	$\frac{4}{4}$		Σ = 4
	Ge2	$\frac{4}{4}$	$\frac{4}{4}$	$\frac{4}{4}$				$\frac{4}{4}$	$\Sigma = 4$
	tical Bond	Σ = 2.5	Σ = 2	Σ = 2	Σ = 2	Σ = 2	Σ = 1.75	Σ = 1.75	
Strei	ngth Sums	2.5 > 2					1.75 < 2	1.75 < 2	
	Charge	OVER	СМР	СМР	СМР	CMP	UNDER	UNDER	
com	pensation	CMP					CMP	CMP	

Table S8. Bond valence sums, provided for each crystallographically unique ion, and global instability index (G) values for Cu_2MnGeS_4 and $Cu_4MnGe_2S_7$.

Compound	Space		Bond Vale	ence Sums		G	Structure
	Group	Cu⁺	Mn ^{2+*}	Ge ⁴⁺	S ²⁻	values	Reference
Cu₂MnGeS₄	Pmn2 ₁	(4 <i>b</i>)	(2 <i>a</i>)	(2 <i>a</i>)	S1(2a) 2.04	0.18	T. Bernert,
		1.26	2.04	3.89	S2(2a) 2.07		A. Pfitzner,
					S3(4b) 2.22		Z. Kristallogr.,
							2005, 220 , 968-
							972.
$Cu_4MnGe_2S_7$	Сс	(4 <i>a</i>)	(4 <i>a</i>)	(4 <i>a</i>)	(4a)	0.19	This work
		Cu1 1.27	2.15	Ge1: 3.82	S1 2.10		
		Cu2 1.26		Ge2: 3.82	S2 2.16		
		Cu3 1.29			S3 2.14		
		Cu4 1.30			S4 2.20		
					S5 2.15		
					S6 2.05		
					S7 2.10		

R₀ and b values come from https://www.iucr.org/ data/assets/file/0011/150779/bvparm2020.cif

^{*}The R_0 values were used for the specific oxidation states of the ions except for Mn²⁺, which has an "unchecked"/unreliable R_0 value. In the case of Mn, we used the value for the unspecified oxidation state, R_0 =2.20 Å, which can also be found in the following reference: N. E. Brese, M. O'Keeffe, *Acta Cryst.* 1991, **B47**, 192-197.

Table S9. The electronic bandgaps at different k-points using the PBE and HSE06 functional in Cu₂MnGeS₄.

K-point	E _g PBE (eV)	E _g HSE06 (eV)	ΔE _g (eV)
(0, 0, 0)	0.6	1.9	1.3
(1/2, 0, 0)	1.3	3	1.7
(1/2, 1/2, 0)	1.8	3.4	1.6
(0, 1/2, 0)	0.8	2.2	1.4
(0, 0, 1/2)	0.8	2.3	1.5
(1/2, 0, 1/2)	1.4	3.1	1.7
(1/2, 1/2, 1/2)	1.7	3.2	1.5

Table S10: The electronic bandgaps at different k-points using the PBE and HSE06 functional in Cu₄MnGe₂S₇.

K-point	E _g PBE (eV)	E _g HSE06 (eV)	ΔE _g (eV)
(0, 0, 0)	0.5	1.7	1.2
(1/2, 0, 0)	0.8	2.1	1.3
(0, 1/2, 0)	0.9	2.3	1.4
(1/2, 1/2, 0)	0.9	2.3	1.4
(1/2, 1/2, 1/3)	1	2.2	1.2
(0, 1/2, 1/3)	1.1	2.4	1.3
(1/2, 1/2, 1/3)	1	2.3	1.3

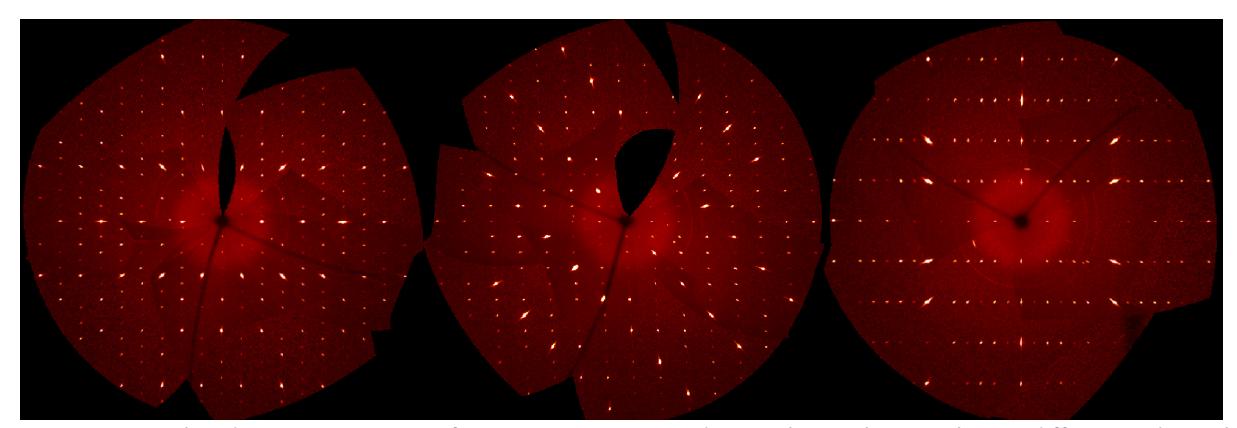


Figure S1. Simulated precession images for $Cu_4MnGe_2S_7$ created using the single-crystal X-ray diffraction data. The (0kl), (h0l), and (hk0) planes in reciprocal space are shown from left to right, respectively. Sharp, bright spots are observed indicative of a single crystal.

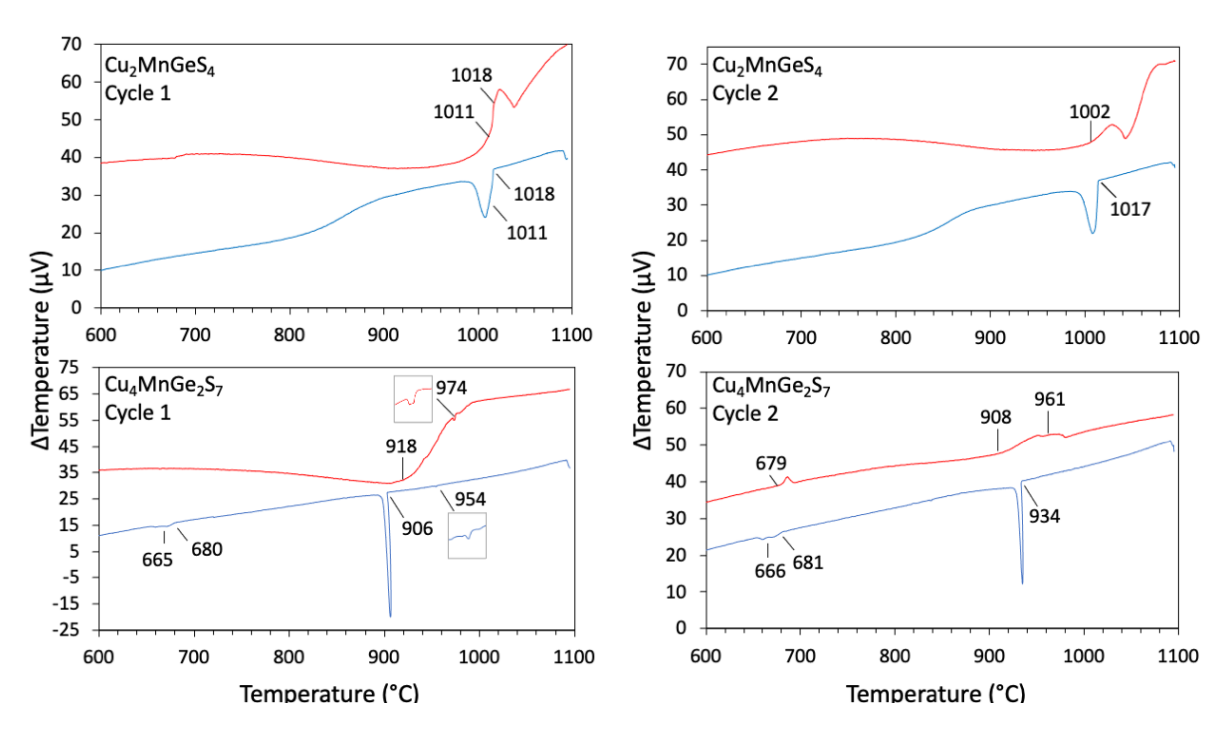


Figure S2. Differential thermal analysis diagrams for Cu₂MnGeS₄ (top) and Cu₄MnGe₂S₇ (bottom). Two cycles were conducted for each experiment.

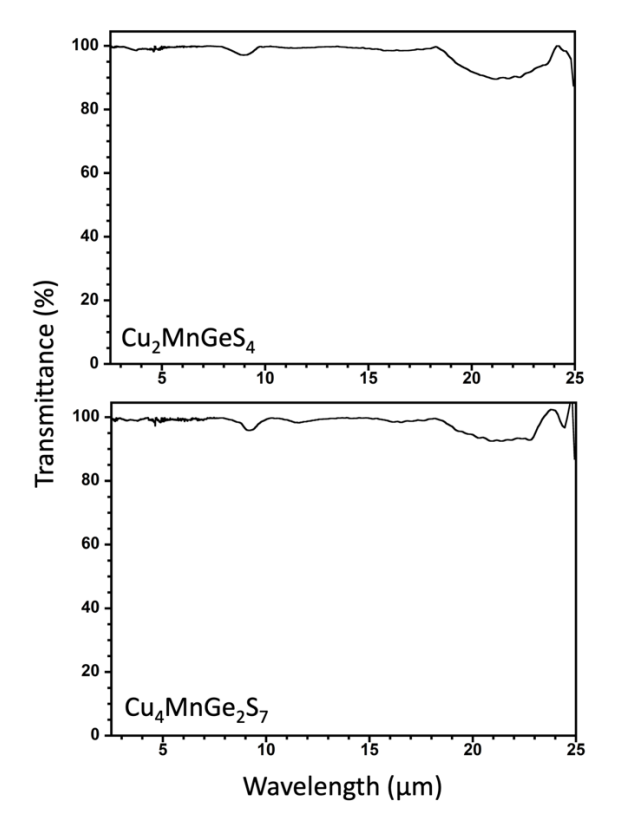


Figure S3. Attenuated total reflectance FT-IR data converted to transmittance for Cu₂MnGeS₄ and Cu₄MnGe₂S₇.